

Chiral twist drives raft formation and organization in membranes composed of rod-like particles

Louis Kang^{a,1} and Tom C. Lubensky^a

^aDepartment of Physics & Astronomy, University of Pennsylvania, Philadelphia, PA 19104

Edited by David A. Weitz, Harvard University, Cambridge, MA, and approved November 21, 2016 (received for review August 25, 2016)

Lipid rafts are hypothesized to facilitate protein interaction, tension regulation, and trafficking in biological membranes, but the mechanisms responsible for their formation and maintenance are not clear. Insights into many other condensed matter phenomena have come from colloidal systems, whose micron-scale particles mimic basic properties of atoms and molecules but permit dynamic visualization with single-particle resolution. Recently, experiments showed that bidisperse mixtures of filamentous viruses can self-assemble into colloidal monolayers with thermodynamically stable rafts exhibiting chiral structure and repulsive interactions. We quantitatively explain these observations by modeling the membrane particles as chiral liquid crystals. Chiral twist promotes the formation of finite-sized rafts and mediates a repulsion that distributes them evenly throughout the membrane. Although this system is composed of filamentous viruses whose aggregation is entropically driven by dextran depletants instead of phospholipids and cholesterol with prominent electrostatic interactions, colloidal and biological membranes share many of the same physical symmetries. Chiral twist can contribute to the behavior of both systems and may account for certain stereospecific effects observed in molecular membranes.

membrane rafts | liquid crystals | chirality | self-assembly | colloids

Filamentous viruses have proved to be a fruitful colloidal system (1–19). They serve as monodisperse, rigid, and chiral rods that are $\sim 1 \mu\text{m}$ in length and interact effectively through hard-core repulsion (2, 7). When suspended in an aqueous solution at increasing concentrations, they transition from a disordered isotropic phase to a cholesteric (chiral nematic) phase characterized by alignment along a director field that twists with a preferred handedness and wavelength (1, 6). The addition of a nonadsorbing polymer such as dextran induces lateral virus–virus attraction via the depletion interaction (10, 12, 20, 21). The viruses self-assemble into monolayers that exhibit fluid-like dynamics internally (10) and sediment to the bottom of glass containers, which are coated with a polyacrylamide brush to suppress depletion-induced virus-wall attractions (22). The rich physics and phenomenology of membranes formed from single-virus species have been thoroughly studied (8–17, 19). However, two-species membranes demonstrate a novel set of behaviors that are not adequately understood (18). We review these behaviors now before describing a theory that can explain them.

fd-Y21M and M13KO7, which we shorten to *fd* and M13 for convenience, are two species of filamentous virus that have slightly different lengths and form cholesteric phases of opposite handednesses (Table 1 and Fig. 14). Membranes composed of both *fd* and M13 viruses are circular with interior particles aligned largely perpendicularly to the membrane plane and edge particles tilted azimuthally, as in single-species membranes (13). At low dextran concentrations, the two species are fully mixed, and at high dextran concentrations, the two are fully phase separated with M13 viruses surrounding a single *fd* domain (Fig. 1B and D). At intermediate concentrations, membranes exhibit partial phase separation with several smaller circular rafts of *fd* viruses distributed within a mixed background of both species (Fig. 1C).

Particle tracking experiments show that *fd* viruses diffuse in and out of these rafts (18), allowing for equilibration to a thermodynamically preferred raft size over ~ 24 h (Fig. 1E). Polarized light microscopy suggests that the raft system has a chiral structure, with particles tilting around the interfaces between rafts and background membrane and around the membrane edge (Fig. 1F). Finally, the rafts are distributed homogeneously throughout the membrane and never coalesce, indicating a long-ranged repulsion between rafts (Fig. 1G). This interaction can be measured quantitatively by bringing two rafts close together with optical traps and tracking their trajectories upon release of the traps (18).

The simplicity of this colloidal membrane system allows us to study it theoretically with a model built from established physical principles and experimentally meaningful parameters. Its components have well-characterized interactions: Dextran molecules act as depletants that interact with viruses through hard-body interactions (10, 12, 20, 21, 26), and the hard-body interactions between viruses can be coarse grained as the Frank free energy for chiral liquid crystals (1, 6). We previously used such a model to investigate single-species membranes and succeeded in reproducing a variety of structural, dynamical, and phase phenomena with a single set of realistic parameter values (19). Extending the model to the two-species system will demonstrate how the intriguing behaviors depicted in Fig. 1 emerge from Frank free energy, depletant entropy, and mixing entropy.

The fundamental principles we encounter on the colloidal scale may apply to similar but less tractable molecular systems whose particles and interactions share the same physical symmetries. Colloidal systems have permitted the investigation of many quintessential condensed matter phenomena with single-particle resolution and exquisite control. For example, spherical

Significance

Chiral objects are different from their mirror images and have properties that are physically forbidden for achiral objects. We show theoretically how one of these properties, the preference for chiral rods to adopt twisted configurations, generates an array of rafts in membranes formed by rod-like particles. Our theory can predict the composition, size, and interactions of these rafts based on measurable attributes of the rods, and its agreement with experimental data from a virus-based system supports its validity. Moreover, it proposes a mechanism for the stabilization of rafts in cell membranes, which are composed of chiral molecules. These lipid rafts are hypothesized to have important biological functions, and their manipulation may rely on a command of molecular chirality.

Author contributions: L.K. and T.C.L. designed research, performed research, analyzed data, and wrote the paper.

The authors declare no conflict of interest.

This article is a PNAS Direct Submission.

¹To whom correspondence should be addressed. Email: lkang@mail.med.upenn.edu.

This article contains supporting information online at www.pnas.org/lookup/suppl/doi:10.1073/pnas.1613732114/-DCSupplemental.

Table 1. Membrane parameters and their values

Parameter	Variable	Experimental estimate	Source	Model value
<i>fd</i> -Y21M half-length	l_{fd}	430 nm	(18)*	Same
M13KO7 half-length	l_{M13}	560 nm	(18)*	Same
Virus half-length difference	d	130 nm	$l_{M13} - l_{fd}$	Same
Virus diameter		7 nm	(18)	
Virus nearest-neighbor distance	ξ	12 nm	(19)	Same
Virus 2D concentration	c_v	$\sim 9,000 \mu\text{m}^{-2}$	$1/\pi(\xi/2)^2$	$8,500 \mu\text{m}^{-2}$
<i>fd</i> -Y21M Frank constant	K_{fd}	~ 2 pN	(1) ^{†,‡}	4 pN
M13KO7 Frank constant	K_{M13}	~ 4 pN	(6) [‡]	10 pN
<i>fd</i> -Y21M twist wavenumber	q_{fd}	$\sim 0.1 \mu\text{m}^{-1}$	(7) [‡]	$0.11 \mu\text{m}^{-1}$
M13KO7 twist wavenumber	q_{M13}	$\sim -0.5 \mu\text{m}^{-1}$	(6) [‡]	$-0.55 \mu\text{m}^{-1}$
<i>fd</i> -Y21M birefringence	Δn_{fd}	~ 0.008	(8) ^{†,§}	0.011
M13KO7 birefringence	Δn_{M13}	~ 0.008	(8) ^{†,§}	0.011
Dextran concentration	c	$48,000 \mu\text{m}^{-3}$	(18)	Same
Dextran radius	a	~ 25 nm	(23–25) [¶]	Same
Temperature	T	22 °C	(18)	Same

*Half the end-to-end length estimated from contour lengths and persistence lengths.

[†] Measured for *fd*-wt virus.

[‡] Imprecise estimates extrapolated to membrane virus concentration $\sim 200 \text{ mg} \cdot \text{mL}^{-1}$ (corresponding to $c_v \sim 9,000 \mu\text{m}^{-2}$) based on concentration-dependent behavior of *fd*-wt suspensions (1).

[§] Assuming membrane nematic order parameter of 1 and virus concentration $\sim 200 \text{ mg} \cdot \text{mL}^{-1}$ (corresponding to $c_v \sim 9,000 \mu\text{m}^{-2}$).

[¶] Hydrodynamic radii for dilute solutions of 500 kDa dextran, whereas our experiments are in the semidilute regime.

colloids exhibit crystal nucleation (27, 28) and glassy dynamics (29, 30); the addition of an isotropic attraction with depletants allows them to demonstrate liquid–gas phase separation (31), thermal capillary waves (32), and wetting (33). And in addition to the aforementioned work in which filamentous viruses form nematic and cholesteric liquid crystal phases, plate-like and rod-like colloids have shed insight on columnar and smectic liquid crystal phases, respectively (34, 35). Phospholipid fluid membranes are another important soft-matter system; however, due to our inability to directly visualize real-time dynamics of lipid bilayers at the nanometer scale, many processes remain poorly understood. Following the analogy between colloids and molecular substances, our theoretical investigation of two-component colloidal membranes may provide new, universal understanding about membrane rafts, which have been observed in experimental phospholipid membranes (36, 37) but remain controversial in the case of biological membranes (38).

As shown in previous work (39, 40) based on phenomenological models, the difference in chirality between two coexisting phases, which favors different twist rates of viruses relative to membrane normals, is the primary driver of raft formation in viral membranes. When two achiral phases coexist, the interface separating them has a positive line tension (or surface tension in three dimensions) that favors the smallest possible interfacial length (or area). Chirality difference introduces an effective negative contribution to the line tension, which for large enough difference becomes negative and favors as much interfacial length as possible. Finite-size rafts are a result of the competition between negative line tension and either repulsive interaction between segments of interface or interfacial curvature energy. The repulsive energy between rafts as they approach each other arises from compression of the twist in the membranes' background phase. The formation of rafts and their mutual interaction follow these fundamental physics in our calculations that are based on the particular depletion physics of viral rafts.

The next few sections describe, respectively, the process of phase separation that generates raft and background phases, the organization of the raft phase into domains with a preferred size and chiral structure, and the repulsion between rafts mediated

by the chiral structure of the background phase. Each section includes theoretical development, results, and comparison with experimental data. In the last section, we discuss the assumptions made by our theory, its contribution to the literature on heterogeneous membranes, and implications for phospholipid membranes.

Phase Separation Between Virus Species

We start by investigating the separation of membrane particles into two phases, one that we call the “background” phase containing mostly M13 viruses completely surrounding the other that we call the “raft” phase containing *fd* viruses, in accordance with experiment (Fig. 1). The structure of the phases, including the number and size of rafts present, does not yet concern us. We assume a large circular membrane of radius $R_t \rightarrow \infty$ and henceforth ignore effects of the outer boundary. The degree of phase separation is parameterized by α^2 , the area fraction of the raft phase (Fig. 2A). It ranges between $\alpha^2 = 0$, which corresponds to complete mixing, and $\alpha^2 = \alpha_t^2$, which corresponds to complete phase separation. α_t^2 is determined experimentally by the fraction of *fd* viruses provided in the initial suspension. For intermediate values of α^2 , some *fd* particles leave the raft and enter the background, producing a partially mixed background phase containing both viruses.

Competition between two factors determines the degree of phase separation. Thermal forces encourage the depletants to explore as much physical space as possible. To do so, they must minimize the volume excluded to their centers of mass by the membrane, which can be accomplished by separating viruses of different lengths into different phases. A shorter *fd* particle produces more excluded volume when surrounded by longer M13 particles (Fig. 2B). For depletant particles small compared with the dimensions of the membrane, the excluded volume is approximately $V + aA$, where V is the volume of the membrane, A is the surface area of the membrane, and a is the depletant radius (41). Their free energy is calculated via the ideal gas partition function $V_a^N/N!\Lambda^{3N}$ applied to N depletant molecules, where Λ is their thermal de Broglie wavelength. The volume available to the depletants can be written as $V_a = V_t - V - aA$, where $V_t \gg V$ is the total volume of the virus-and-depletant

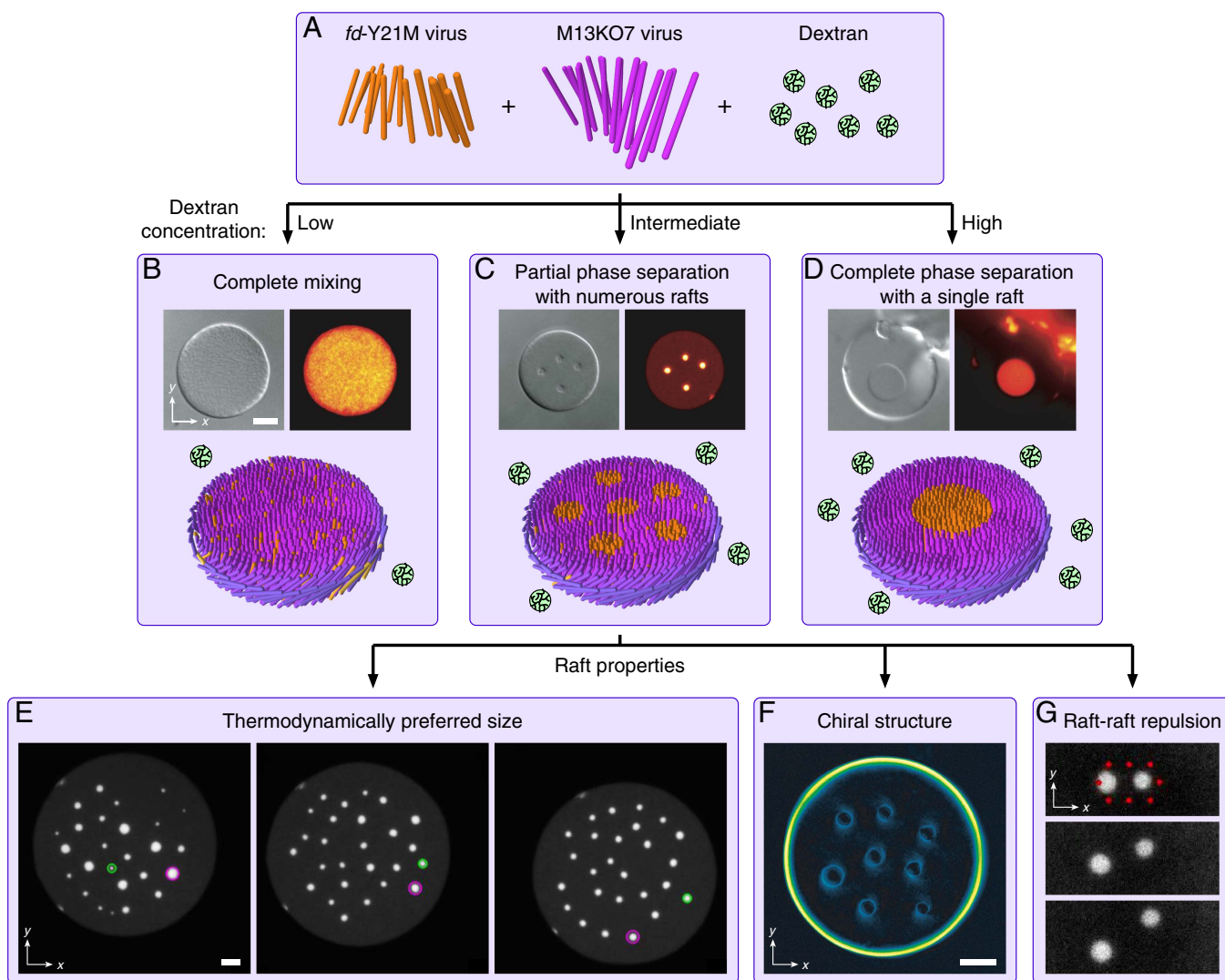


Fig. 1. Overview of two-species colloidal membrane experiments. (A) Virus particles and dextran molecules act as rod-shaped colloids and spherical depletants, respectively. *fd* viruses are shorter and prefer right-handed twist. M13 viruses are longer and prefer left-handed twist. (B–D) Differential interference contrast image (Top Left), fluorescence image with *fd* labeled (Top Right), and schematic (Bottom) of colloidal membranes. (B) At a low dextran concentration of $41,000 \mu\text{m}^{-3}$, the two virus species completely mix. (C) At an intermediate dextran concentration of $46,000 \mu\text{m}^{-3}$, several smaller rafts of *fd* virus form in a partially phase-separated background. (D) At a high dextran concentration of $62,000 \mu\text{m}^{-3}$, the two virus species completely phase separate. (E) Rafts exchange rods with the background membrane to attain a thermodynamically preferred size. Fluorescence images with *fd* labeled are taken 6.7 h apart. Green and purple circles track two rafts that start, respectively, smaller and larger than the preferred raft size. (F) Viruses adopt a twisted chiral structure. Shown is an LC-PolScope birefringence map with pixel brightness representing retardance, which indicates virus tilt toward the membrane plane. (G) Rafts repel one another. Fluorescence images with *fd* labeled are taken 5 s apart. Two optical plows consisting of multiple light beams (red circles) bring two rafts together and are then switched off. (All scale bars, $5 \mu\text{m}$.) Experimental data and methods are reported in ref. 18. Schematics are not drawn to scale. Microscopy images were reprinted by permission from Macmillan Publishers Ltd. (18).

suspension (42). Ignoring constant terms, the depletant free energy is generically

$$F_{\text{dep}} = -NT \log \frac{V_i - V - aA}{V_t} \approx cT(V + aA), \quad [1]$$

where c is the depletant concentration and T is the temperature. We use units in which the Boltzmann constant is unity.

However, thermal forces also encourage binary fluids to adopt disordered phases in which the two species are mixed. This tendency is described quantitatively by the entropy of mixing (43). As depicted in Fig. 2A, the mixed background phase of total area $(1 - \alpha^2)\pi R_t^2$ is formed from an area $(\alpha_t^2 - \alpha^2)\pi R_t^2$ of *fd* viruses and an area of $(1 - \alpha_t^2)\pi R_t^2$ of M13 viruses, yielding respective area fractions

$$\phi_{fd} = \frac{\alpha_t^2 - \alpha^2}{1 - \alpha^2} \quad \text{and} \quad \phi_{M13} = \frac{1 - \alpha_t^2}{1 - \alpha^2} = 1 - \phi_{fd}. \quad [2]$$

The entropy of mixing per particle of the background phase is

$$s_{\text{mix}} = \phi_{fd} \log \phi_{fd} + \phi_{M13} \log \phi_{M13}. \quad [3]$$

We consider mixing only in the background phase because introducing the longer M13 viruses into the raft phase is disfavored by the depletants. Their surface protrusions would be surrounded by extra excluded volume of order da^2 per M13 particle, unlike the smaller amount of excluded volume of order $d(\xi/2)^2$ per *fd* particle required to introduce the shorter *fd* viruses into the background phase (Fig. 2C). $d \equiv l_{M13} - l_{fd}$ is the virus half-length difference, a is the depletant radius, and ξ is the nearest-

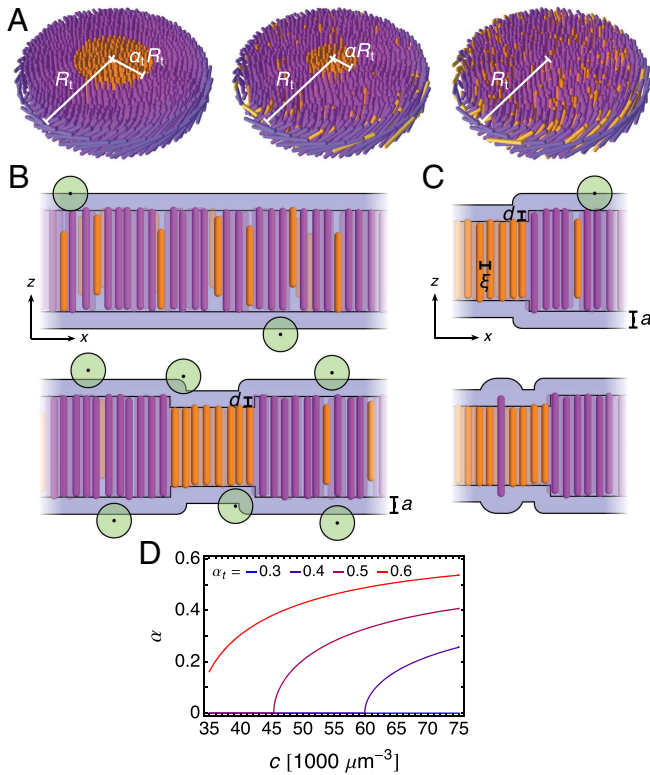


Fig. 2. Phase separation into a raft phase containing only *fd* virus (orange) and a background phase containing both *fd* and M13 (purple) viruses. (A) For a completely phase-separated membrane (Left), the area fraction of the raft phase is $\alpha^2 = \alpha_t^2$; equivalently, if the raft phase formed a single circular domain as depicted, it would have radius $\alpha_t R_t$. As *fd* viruses enter into the M13-rich phase (Center), the area fraction of the raft phase decreases to $\alpha^2 < \alpha_t^2$. For a completely mixed membrane (Right), $\alpha^2 = 0$. (B) Competition between the entropy of mixing and depletion entropy determines α . At low depletion concentration (Top), the mixed state is entropically preferred. Phase separation reduces the excluded volume and is preferred at high depletion concentration (Bottom). Green circles represent depletants and blue regions represent the excluded volume. (C) Introducing a shorter virus into a sea of longer ones (Top) increases the excluded volume less than introducing a longer virus into a sea of shorter ones (Bottom). (D) α for various α_t and depletion concentrations c (Eq. 5). Values for other parameters are provided in Table 1. Schematics are not drawn to scale.

neighbor virus separation (Table 1). We thus ignore mixing in the raft phase due to these asymmetric effects of surface convexity and concavity on the depletion free energy (the origins of these effects are explored further in Fig. S1 and in Landau Coefficients for Phase Separation).

Combining the mixing entropy Eq. 3 and the depletion free energy Eq. 1, which respectively disfavor and favor phase separation, gives the free energy

$$\frac{F_{\text{sep}}}{\pi R_t^2 T} = c_v \left[(1 - \alpha_t^2) \log \frac{1 - \alpha_t^2}{1 - \alpha^2} + (\alpha_t^2 - \alpha^2) \log \frac{\alpha_t^2 - \alpha^2}{1 - \alpha^2} \right] + 2cd(\alpha_t^2 - \alpha^2), \quad [4]$$

where c is the 3D depletant concentration and c_v is the 2D virus concentration in the membrane. Minimizing F_{sep} with respect to α produces the result

$$\alpha = \begin{cases} \sqrt{\frac{\alpha_t^2 - e^{-2cd/c_v}}{1 - e^{-2cd/c_v}}} & cd/c_v \geq \log 1/\alpha_t \\ 0 & cd/c_v \leq \log 1/\alpha_t, \end{cases} \quad [5]$$

where c is the 3D depletant concentration, c_v is the 2D virus concentration in the membrane, and d is the half-length difference between the two species. In Fig. 2D, $\alpha(c)$ is plotted for various α_t s, using values in Table 1. For each α_t , there is complete mixing ($\alpha = 0$) below a critical depletion concentration $(c_v/d) \log 1/\alpha_t$. Above this critical c , the system partially phase separates and approaches complete phase separation for $c \rightarrow \infty$. This behavior qualitatively agrees with experimental results in Fig. 1 B–D over the experimental range of depletion concentrations c .

Raft Organization and Structure

Assuming we are in the regime $cd/c_v > \log 1/\alpha_t$ in which rafts exist, we now analyze their structure. Eq. 5 determines the total amount of *fd* virus sequestered into the raft phase by setting the value of α , but does this phase form a single large raft or several smaller rafts (Fig. 3A)? And how are the virus particles aligned? We will see that these questions are related via the natural tendency of chiral rods to adopt twisted configurations. To answer them, we need to derive the structural free energy of the membrane.

We take the membrane of radius $R_t \rightarrow \infty$ to be approximately tiled by circularly symmetric domains of radius R (Fig. 3B), as in the muffin-tin approximation of solid-state physics (44). There are R_t^2/R^2 domains and the total membrane free energy is

$$F_{\text{struct}} = \frac{R_t^2}{R^2} F_{\text{domain}}, \quad [6]$$

where F_{domain} is the free energy of a single domain, which contains one raft of radius αR . The *fd* particles point vertically at the center of the raft and twist azimuthally with one handedness to their interface with the background, where they attain twist angle θ_0 . The background particles, which are mostly M13 with a smaller amount of *fd*, twist with opposite handedness from θ_0 at the interface to 0 at the domain edge, where the next domain would begin (Fig. 3C). Once the membrane separates into its thermodynamically preferred raft and background phases, we assume zero net particle current between the phases and between each phase and the aqueous environment. We also assume that the 2D particle concentration c_v in the membrane is constant. Thus, the volume of each phase is conserved, so any effects of depletion must act only on the surface area of the membrane (Eq. 1). For mathematical tractability, we assume the particles do not twist very much, so their tilt angle satisfies $\theta \ll 1$, and the two virus species have similar half-lengths l_{fd} and l_{M13} , so their half-length difference satisfies $d \ll l_{fd} \approx l_{M13}$. As calculated in ref. 19, virus position fluctuations perpendicular to the membrane are strongly suppressed in the $\theta \ll 1$ limit, so the thicknesses of the raft and background phases are simply $2l_{fd} \cos \theta$ and $2l_{M13} \cos \theta$, respectively.

F_{domain} consists of three components. First, interfaces between raft and background have a half-height difference of approximately d . These vertical offsets, which appear as “corners” in Fig. 3D, contribute additional membrane surface area and, through the depletion free energy Eq. 1, produce an effective interfacial line tension proportional to d . Second, virus tilt away from the membrane normal also increases the membrane surface area and, also through depletion, produces an effective alignment energy proportional to θ^2 (Fig. 3E). Third, the virus particles behave as chiral nematic liquid crystals (1, 6). That is, each species prefers to be aligned in a twisted configuration with wavenumber q , where the sign of q indicates the chirality of twist (positive corresponds to right handed) and $2\pi/|q|$ is the wavelength. The energetic cost of deviations from this preferred configuration is given by the Frank free energy (45):

$$F_{\text{Frank}} = K \int d^2 \mathbf{x} \, l \cos \theta [(\nabla \cdot \mathbf{n})^2 + (\nabla \times \mathbf{n})^2 - 2q \mathbf{n} \cdot \nabla \times \mathbf{n}]. \quad [7]$$

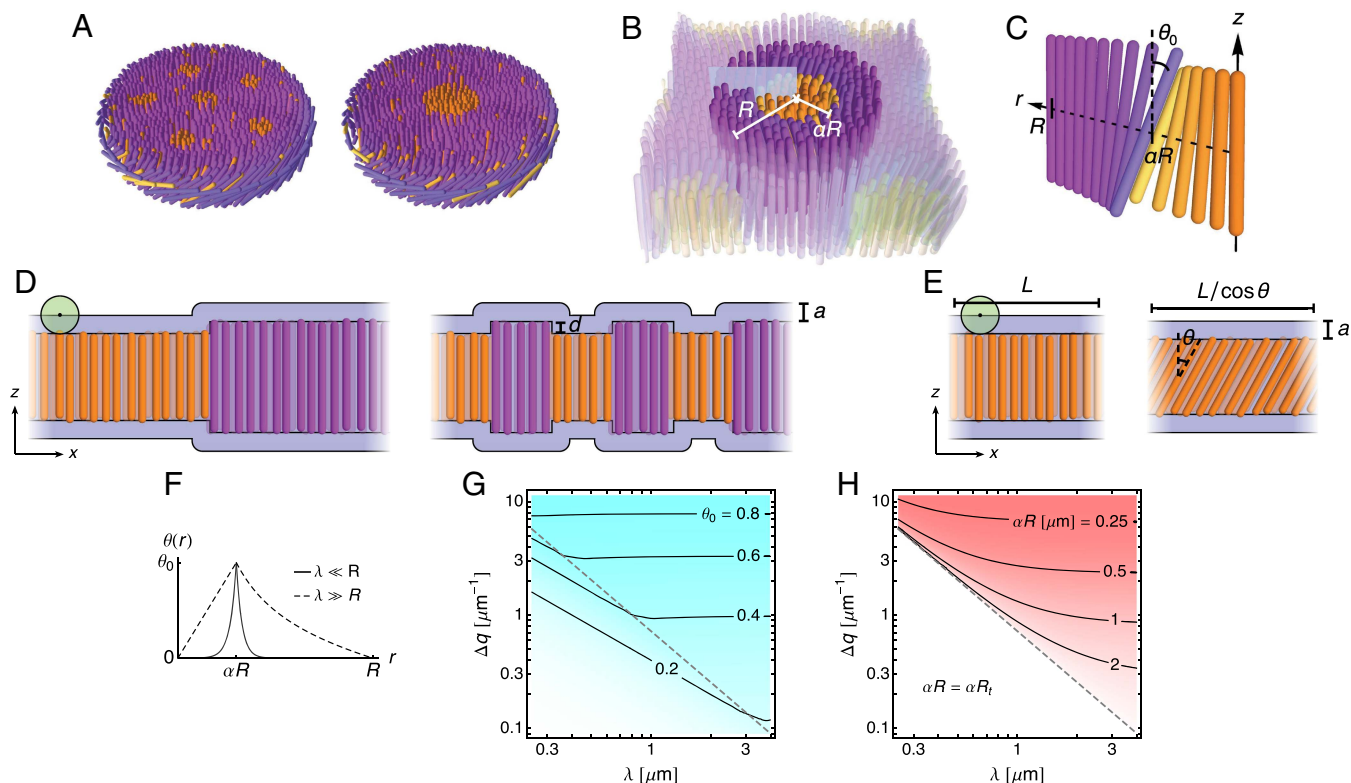


Fig. 3. Raft size and chiral structure. (A) Schematics of two membranes with the same degree of phase separation and thus the same raft area fraction α^2 containing either several smaller rafts (Left) or one larger raft (Right). (B) A single circular domain with a single circular raft is repeated to approximately tile the membrane. (C) Structure of the domain along the light blue plane in B. Along the radial coordinate r , the fd viruses (orange) twist from $\theta(0) = 0$ to $\theta(\alpha R) = \theta_0$ at the raft-background interface with one handedness, and the background viruses, containing mostly M13 virus (purple), twist from $\theta(\alpha R) = \theta_0$ to $\theta(R) = 0$ at the domain edge with the other handedness. (D and E) The effect of depletants (green circles) on raft structure and organization. (D) Between two membranes of equal volume, the one with more interface between raft and background (Right) has greater excluded volume (blue), leading to an interfacial line tension proportional to d . (E) Between two membranes of equal volume, the one whose viruses are tilted at angle θ (Right) has greater excluded volume, leading to a free energy term proportional to θ^2 to leading order. (F) Tilt angle $\theta(r)$ (Eq. 11) for domains whose common twist penetration depth $\lambda \equiv \lambda_1 \approx \lambda_2$ is much less or much greater than their radius R . (G) Maximum twist angle θ_0 (Eq. 12) as a function of λ and the twist wavenumber difference $\Delta q \equiv q_1 - q_2$. Darker cyan indicates larger θ_0 . (H) Raft radius αR as a function of λ and Δq , calculated numerically. Darker red indicates smaller αR . We assume the large membrane limit $R_t \rightarrow \infty$. The maximum raft radius αR_t corresponds to a membrane having only a single raft, a regime separated by a gray dashed line from membranes with multiple smaller rafts (Eq. 15). This line is reproduced in G. For G and H, $\alpha = 0.3$ and values for other parameters are provided in Table 1. Schematics are not drawn to scale.

\mathbf{n} is the nematic director, K is the 3D Frank elastic constant in the one-constant approximation, q is the preferred twist wavenumber associated with intrinsic chirality of the constituent particles, l is the particle half length, and θ is the particle tilt angle. For raft domains depicted in Fig. 3 B and C, the nematic director is circularly symmetric and tilts away from the membrane normal in the negative azimuthal direction:

$$\mathbf{n}(r) = -\sin \theta(r) \hat{\phi} + \cos \theta(r) \hat{z}. \quad [8]$$

The complete derivation of the F_{domain} is given in [Derivation of the Single-Domain Free Energy](#), and it leads to the structural free energy

$$\begin{aligned} \frac{F_{\text{struct}}}{4\pi caT} = & \frac{R_t^2}{R^2} \left\{ d\alpha R - [\lambda_1^2 q_1 - \lambda_2^2 q_2] \alpha R \theta_0 + \frac{1}{2} [\lambda_1^2 + \lambda_2^2] \theta_0^2 \right. \\ & + \int_0^{\alpha R} dr \left[\frac{1}{2} r \theta^2 + \frac{\lambda_1^2}{2} \left(r (\partial_r \theta)^2 + \frac{\theta^2}{r} \right) \right] \\ & \left. + \int_{\alpha R}^R dr \left[\frac{1}{2} r \theta^2 + \frac{\lambda_2^2}{2} \left(r (\partial_r \theta)^2 + \frac{\theta^2}{r} \right) \right] \right\}. \quad [9] \end{aligned}$$

The subscripts 1 and 2 refer to raft and background phases, respectively. An important length scale $\lambda_j \equiv \sqrt{K_j l_j / caT}$ arises

from comparing the Frank twist and depletion contributions to the free energy, where $j \in \{1, 2\}$. The latter penalizes nonzero $\theta(r)$ and the former penalizes gradients in $\theta(r)$, so λ_j acts like a twist penetration lengthscale. Because only fd viruses compose rafts, $q_1 = q_{fd}$ and $\lambda_1 = \sqrt{K_{fd} l_{fd} / caT}$. The corresponding expressions for the background must account for a mixture of virus species. Experiments demonstrate that cholesteric mixtures of fd -wt and fd viruses have intermediate twist wavenumbers that linearly interpolate between their pure values as a function of relative concentration (7). We assume that the same behavior applies here to Frank constants and twist wavenumbers for fd and M13 viruses:

$$q_2 = \frac{1 - \alpha_t^2}{1 - \alpha^2} q_{M13} + \frac{\alpha_t^2 - \alpha^2}{1 - \alpha^2} q_{fd} \quad \text{and} \quad \lambda_2 = \sqrt{\frac{K_2 l_{M13}}{caT}},$$

where $K_2 = \frac{1 - \alpha_t^2}{1 - \alpha^2} K_{M13} + \frac{\alpha_t^2 - \alpha^2}{1 - \alpha^2} K_{fd}$. [10]

Experimental estimates for K and virus half-length l are of the same order of magnitude for the two species (Table 1). For better mathematical insight and clearer presentation of results, we sometimes imagine that they are equal, so the two phases share the same $\lambda \equiv \lambda_1 \approx \lambda_2$. Another important parameter is

$\Delta q \equiv q_1 - q_2$, the difference between the chiral wavenumbers of the raft and background.

Minimization of F_{struct} over the tilt angle $\theta(r)$ and the domain radius R yields the thermodynamically preferred membrane structure. We first minimize over $\theta(r)$ with the boundary conditions $\theta(0) = 0$, $\theta(\alpha R) = \theta_0$, and $\theta(R) = 0$,

$$\theta(r) = \begin{cases} \theta_0 \frac{I_1(s_1)}{I_1(\alpha S_1)} & 0 \leq r \leq \alpha R \\ \theta_0 \frac{K_1(s_2)/K_1(S_2) - I_1(s_2)/I_1(S_2)}{K_1(\alpha S_2)/K_1(S_2) - I_1(\alpha S_2)/I_1(S_2)} & \alpha R \leq r \leq R, \end{cases} \quad [11]$$

where I_ν and K_ν are modified Bessel functions of the first and second kind, respectively, of order ν (the latter should not be confused for Frank constants). Distances are rescaled by the twist penetration depths as $s_j = r/\lambda_j$ and $S_j = R/\lambda_j$, for $j \in \{1, 2\}$. Solving the Euler-Lagrange equation is described in *Calculation of the Virus Tilt Angle*. Eq. 11 is plotted in Fig. 3F. If the common twist penetration depth λ is much less than R , then the twist is exponentially localized to the interface between raft and background, but if it is much greater than R , then the twist $\partial_r \theta$ extends uniformly throughout the membrane.

We then substitute Eq. 11 into Eq. 9, perform the integrals over r , and minimize over θ_0 , the tilt angle at the interface:

$$\theta_0 = \frac{\lambda_1^2 q_1 - \lambda_2^2 q_2}{\lambda_1 \frac{I_0(\alpha S_1)}{I_1(\alpha S_1)} + \lambda_2 \frac{K_0(\alpha S_2)/K_1(S_2) + I_0(\alpha S_2)/I_1(S_2)}{K_1(\alpha S_2)/K_1(S_2) - I_1(\alpha S_2)/I_1(S_2)}}. \quad [12]$$

This equation is plotted in Fig. 3G. The magnitude of θ_0 increases with λ and Δq , and its sign is determined by the sign of Δq .

Substituting Eq. 12 back into F_{struct} yields

$$\frac{F_{\text{struct}}}{4\pi R_t^2 c a T} = \frac{\alpha}{R} \left\{ d - \frac{1}{2} \frac{(\lambda_1^2 q_1 - \lambda_2^2 q_2)^2}{\lambda_1 \frac{I_0(\alpha S_1)}{I_1(\alpha S_1)} + \lambda_2 \frac{K_0(\alpha S_2)/K_1(S_2) + I_0(\alpha S_2)/I_1(S_2)}{K_1(\alpha S_2)/K_1(S_2) - I_1(\alpha S_2)/I_1(S_2)}} \right\}, \quad [13]$$

which depends on the free parameter R only through S_1 and S_2 . By minimizing over R , we numerically calculate the preferred raft radius αR , remembering that α was determined in the previous section. Fig. 3H shows that at low λ and Δq , R adopts its maximum value, R_t , so the membrane contains one large raft. As Δq increases past a critical value, R prefers a finite value and the raft phase separates into several smaller rafts of radius αR . For constant Δq , increasing λ —or equivalently decreasing c —leads to more numerous, smaller rafts, which qualitatively agrees with experimental observations in Fig. 1 C and D. Note that the chirality inversion $q_1 \rightarrow -q_1$ and $q_2 \rightarrow -q_2$ yields the mirror-image configuration $\theta(r) \rightarrow -\theta(r)$ via Eqs. 11 and 12 with the same free energy Eq. 13.

A large chiral twist wavenumber difference Δq indicates the proclivity of *fd* and M13 viruses to twist back and forth with opposite handednesses; however, depletants favor particle alignment perpendicular to the membrane. A large number of small rafts can satisfy both tendencies, because the particles can twist back and forth over short distances while largely maintaining perpendicular alignment. In opposition is the positive interfacial line tension also generated by depletion, which prefers a small number of large rafts to reduce the total interfacial length between raft and background phases. The competition between these factors sets the raft size, which we can see explicitly by expanding the free energy to leading orders in R^{-1} , corresponding to the

phase transition between single- and multiple-raft membranes. With the simplification $\lambda \equiv \lambda_1 \approx \lambda_2$, Eq. 13 becomes

$$\frac{F_{\text{struct}}}{4\pi R_t^2 c a T} \sim \frac{\alpha}{R} \left\{ d - \frac{1}{4} \lambda^3 \Delta q^2 + \frac{3}{32} \frac{\lambda^5 \Delta q^2}{\alpha^2 R^2} + \frac{1}{4} \lambda^3 \Delta q^2 e^{-2(1-\alpha)R/\lambda} \right\}. \quad [14]$$

Thus, virus chirality appends a correction term to the bare interfacial tension to produce the effective interfacial line tension $2caT(d - \lambda^3 \Delta q^2/4)$. When this effective tension becomes negative, the system prefers multiple smaller rafts instead of a single large raft to increase the total interfacial length. The critical dashed line of Fig. 3H occurs when it equals zero and is thus given by

$$|\Delta q| = 2d^{1/2} \lambda^{-3/2}. \quad [15]$$

In the multiple-raft regime where $|\Delta q|$ exceeds this critical value, the preferred raft size is

$$\alpha R \sim \sqrt{\frac{9}{32} \frac{\lambda^5 \Delta q^2}{\frac{1}{4} \lambda^3 \Delta q^2 - d}}, \quad [16]$$

indicating a second-order phase transition. Note that Eq. 14 is analogous to the free energy of the 2D Frenkel-Kontorova model around the commensurate-incommensurate transition, with the first two terms corresponding to an effective interfacial line tension between rafts and background, the third corresponding to what can be interpreted as an effective interfacial bending energy, and the fourth corresponding to raft-raft repulsion (43, 46). The higher-order terms prevent a negative effective interfacial tension from decreasing the raft size to 0 and set the preferred size, Eq. 16.

To assess the validity of our model, we can compare measurements of optical retardance (Fig. 1F) to values calculated by our model. When polarized light passes through a birefringent material, the “ordinary” and “extraordinary” components propagate at different speeds, leading to a phase difference called retardance that we measure in wavelengths. For our membranes, it is approximately given by $D = 2\Delta n l \sin^2 \theta$ and is thus an indirect measure of the tilt angle θ (47). The raw calculated retardance profiles are convolved with a Gaussian of width 0.13 μm representing the microscope’s resolution function, exactly as previously reported (8). Fig. 4 shows good agreement between theoretical and experimental retardance profiles, using the physically reasonable birefringence values reported in Table 1.

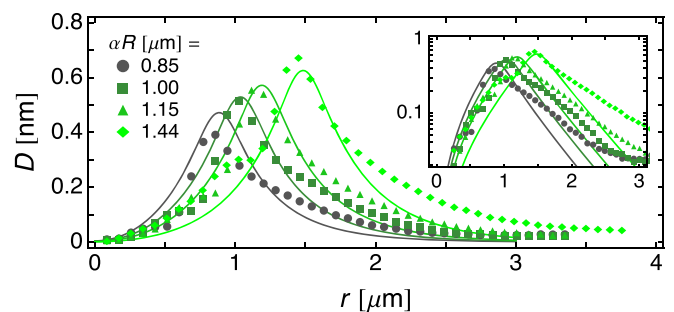


Fig. 4. Retardance values D for rafts of various radii αR . The points indicate experimental data and the lines indicate theoretical results calculated with $\alpha_t = 0.5$ and the parameter values in Table 1, corresponding to twist penetration depth $\lambda \sim 0.8 \mu\text{m}$ and chiral wavenumber difference $\Delta q = 0.5 \mu\text{m}^{-1}$. α is given by Eq. 5 and R is adjusted to produce rafts of different radii. Experimental data and methods are reported in ref. 18.

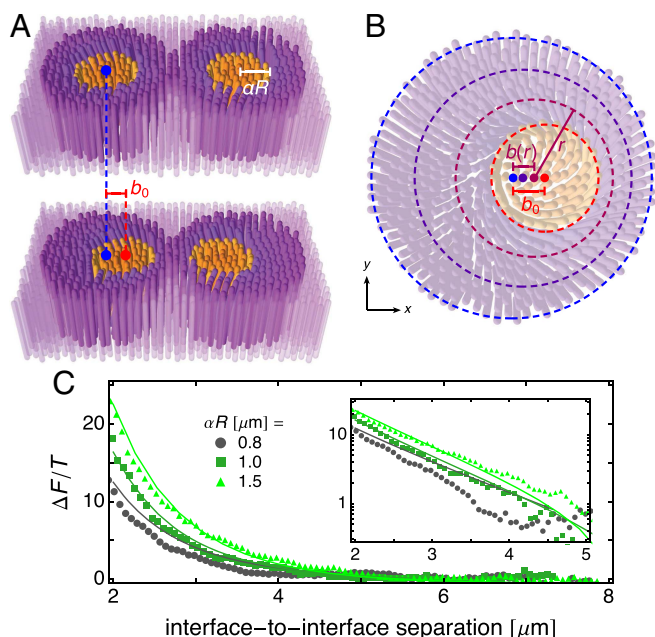


Fig. 5. Raft-raft repulsion. (A) The approach of two rafts is modeled as raft shifts b_0 with respect to their circular tiling domains. (B) Shifted polar coordinate system of the background membrane (Eq. 17). Dashed lines indicate curves of constant r from $r = \alpha R$ (red) to $r = R$ (blue), which are circles of radius r whose centers (dots) lie at $x = b(r)$ and $y = 0$. (C) Raft-raft repulsion energy ΔF divided by temperature T for rafts of various radii αR . The points indicate experimental data and the lines indicate theoretical results calculated with $\alpha_t = 0.5$ and the parameter values in Table 1, corresponding to twist penetration depth $\lambda \sim 0.8 \mu\text{m}$ and chiral wavenumber difference $\Delta q = 0.5 \mu\text{m}^{-1}$. α is given by Eq. 5 and R is adjusted to produce rafts of different radii. Experimental data and methods are reported in ref. 18. Schematics are not drawn to scale.

Raft-Raft Repulsion

To model the interaction between two neighboring rafts as they approach each other, we shift each circular raft within its circular tiling domain off center by a distance b_0 toward each other (Fig. 5A). To accomplish this, the background membrane must be deformed; for simplicity, we assume that the rafts themselves are unchanged by this shift. We parameterize the deformation by a shift profile $b(r)$ such that Cartesian coordinates are given in terms of shifted polar coordinates by

$$x = r \cos \phi + b(r) \quad \text{and} \quad y = r \sin \phi. \quad [17]$$

In other words, the curves of constant r are nested non-concentric circles of radius r centered at $x = b(r)$ and $y = 0$ (Fig. 5B). Our shift ansatz Eq. 17 breaks circular symmetry into dipolar symmetry, implying that θ can vary with azimuthal angle ϕ and that particles can tilt in the \hat{r} direction. To dipolar order, $\theta(r, \phi) = \theta(r) + \vartheta(r) \cos \phi$, where $\vartheta(r)$ is the dipolar tilt component. We must carefully recalculate terms in the single-domain free energy F_{domain} that would be changed by this coordinate transformation:

$$\frac{F_{\text{shift}}}{2\alpha T} = \int_{\alpha R}^R dr \int_0^{2\pi} d\phi h_r h_\phi \times \left\{ \frac{1}{2} \theta^2 + \frac{\lambda_2^2}{2} [(\nabla \cdot \mathbf{n})^2 + (\nabla \times \mathbf{n})^2] \right\}. \quad [18]$$

h_r and h_ϕ are scale factors of the coordinate transformation. The evaluation of Eq. 18 is provided in *Calculation of the Raft Shift Free Energy*, where we see that the \hat{r} component of \mathbf{n} can be ignored to leading order in tilt angles. The shift profile

$b(r)$ appears from the scale factors and the spatial derivatives. Because we assume the rafts are unchanged by the deformation, $\theta(\alpha R) = \theta_0$ and $\vartheta(\alpha R) = 0$, corresponding to the unshifted interfacial tilt angle given by Eq. 12. The deformation vanishes at the edge of the tiling domain, so $b(R) = 0$, $\theta(R) = 0$, and $\vartheta(R) = 0$. To calculate the interaction energy between two rafts as a function of separation distance, we impose various shift distances $b_0 = b(\alpha R)$; numerically minimize the free energy over $b(r)$, $\theta(r)$, and $\vartheta(r)$; subtract the energy of the unshifted membrane with $b(r) = 0$; and double the result.

Meanwhile, the repulsive free energy of this two-raft system has been measured experimentally via optical trapping by moving rafts toward each other, releasing them, and tracking their subsequent trajectories (Fig. 1G and ref. 18). Using parameter values given in Table 1, our model agrees well with these measurements for various raft radii αR (Fig. 5C). Thus, despite our relatively simple ansatz, our results quantitatively demonstrate that deformation of the background membrane as two rafts approach each other can explain the observed repulsion between rafts.

Discussion

Our model is designed to emphasize physical relevance and minimize phenomenological contributions. To do so, we ignore many effects that may ultimately produce a more precise description of these colloidal membranes, but in the process add more fit parameters that obscure the underlying generalizable physical principles. For example, the viruses are idealized to be hard rods that form geometrically precise and homogeneous membranes. During phase separation, we disregard the increased translational entropy of the shorter fd viruses when they are embedded within the longer M13 viruses. Furthermore, for mathematical tractability, we expand the membrane free energy to quadratic order in d/l_f and θ , even though the values in Table 1 imply $d/l_f = 0.3$ and $\theta_0 \approx 0.25$.

On the other hand, our conceptual division of raft formation into the two sequential steps of phase separation and raft organization appears to be justified. Numerical minimization of a free energy combining Eqs. 4 and 13 yields results indistinguishable from Figs. 2D and 3H, indicating that the characteristic energy scale of phase separation is much higher than that of raft organization. Moreover, this division is demonstrated in the experimental separation of relaxation timescales. As depicted in Fig. 1E, rafts take ~ 24 h to reach their equilibrium size, but the membrane reaches its equilibrium degree of phase separation much more quickly (the background fluorescence stays constant throughout the three panels). Both processes undergo energetic relaxation through diffusion of the same particles, so their decay timescales scale as $\tau \sim \eta/\varepsilon$, where η is the viscosity and ε is an energy density scale. A larger τ for the process of raft organization corresponds to a smaller ε compared with that of membrane phase separation, which our model explains.

Despite these sweeping simplifications, our model can match measurements with quantitative accuracy while using physically reasonable parameter values. It is consistent with our single-component membrane model that described an independent set of experimental observations (19). Moreover, it provides meaningful insight into the fundamental mechanisms that drive membrane raft formation and organization. Competition between mixing entropy and depletion entropy determines the degree of phase separation of two virus species with different lengths. This competition is independent of virus chirality and can be easily and precisely tuned by adjusting the depletant concentration. A difference in the natural tendency for chiral particles to twist with a preferred handedness and pitch endows the rafts with a chiral structure. This structure stabilizes small rafts against an interfacial line tension that would otherwise promote coarsening to a single raft domain and establishes a preferred depletant-concentration-dependent raft size. The twisted structure of the

background membrane transmits torques and mediates an elastic repulsion between rafts.

Previous theoretical reports have demonstrated that chiral structure can establish a membrane lengthscale, but they differ from our theory in several crucial ways. Some describe single-component smectic-*C* membranes that contain hexagonal cells with only one handedness of twist and arrays of defects at the corners of the cells (48, 49). Selinger et al. (50) investigate membranes formed from racemic mixtures that can form domains of alternating chirality upon spontaneous symmetry breaking. They find a square lattice of domains that also contain defects at their corners. Simultaneously with our work, their theory has been expanded to hexagonal domains without defects and applied to filamentous virus membranes (40). These aforementioned theories are based on phenomenological Landau expansions in the concentration difference between the two chiral components (we show how our model can provide values for Landau coefficients in *Landau Coefficients for Phase Separation*). Complementarily, Xie et al. (39) investigate raft–raft repulsion by directly minimizing the free energy of both raft and background. They highlight the role of background chiral twist and use values for Frank constants (5 pN) and twist wavenumbers ($\sim 3 \mu\text{m}^{-1}$) that are within an order of magnitude of those we use (Table 1). However, they assume well-defined rafts of a particular size, ignoring the processes of phase separation and raft size establishment, and use a phenomenological virus tilt modulus without exploring its physical basis in depletion entropy. In contrast, our theory, which provides a more unified microscopic approach that facilitates comparison with experiments, produces analytical expressions for the chiral raft structure and provides mathematical intuition for raft–raft repulsion via a shift ansatz.

Colloidal membranes composed of viruses share important physical symmetries with their molecular counterparts, even though their characteristic lengthscales and microscopic origins of interactions differ. In fact, a leading-order free energy for rafts in a flat molecular membrane would look very much like Eq. 9. The interfacial line tension between rafts and background would replace the term proportional to d (51, 52). Phases that prefer alignment perpendicular to the membrane plane, such as the biologically relevant L_α phase, would require a θ^2 term (53, 54). Molecular twist would be encapsulated by Frank free energy terms. A generalization of our model that can be applied to other membrane systems is provided in *General Membrane Rafts Formed from Chiral Rod-Like Particles*. Furthermore, experimentally prepared and biological membranes have rafts enriched in

cholesterol compared with the background (55, 56). Cholesterol demonstrates a strong preference for chiral twist—in fact, the chiral nematic, or cholesteric, phase was the first liquid crystalline phase observed in 1888 by Friedrich Reinitzer while investigating cholesteryl esters (57). Hence, we expect a significant difference in chiral wavenumbers Δq that could stabilize smaller rafts.

Our theory contributes to a biologically relevant and poorly understood niche in the rich literature on molecular membranes. It may explain why Langmuir monolayers composed of multiple chiral molecules demonstrate a limit to domain coarsening (58) and biological lipid rafts are believed to have a finite size (59), in contradiction to continuous coarsening predicted by the Cahn–Hilliard model of phase separation (43). Our description of raft–raft repulsion is analogous to the twist-mediated interaction of chiral islands in smectic-*C* films (60–62). It offers an explanation for the mutual repulsion observed between transmembrane protein pores formed by certain antimicrobials, if one imagines that these chiral pores impose phospholipid tilt at their interface with the background membrane (63, 64). Ultimately, the validity of our theory in a particular membrane system hinges on the direct observation of twist, which can be achieved with polarized optical microscopy if the twist penetration depth is at least the wavelength of light (13).

Moreover, phospholipid rafts demonstrate chiral phase behavior that must be explained by a theory attuned to chirality. By either replacing naturally chiral sphingomyelins with a racemic mixture (65) or replacing cholesterol with its enantiomer (66, 67) [although these latter studies disagree with subsequent work (68, 69)], the critical point for phase separation changes. Although for our model parameters phase separation occurs independently from raft organization, other parameter values cause the raft area fraction α^2 to depend on the difference in chiral twist wavenumbers Δq (Fig. S2 and *Chiral Contribution to Phase Separation*). Furthermore, different enantiomers of the same anesthetic molecule have been shown to have different potencies (70–72). Our theory presents a paradigm through which chirality affects physical membrane properties, in accordance with the classic hypothesis that anesthetic molecules disrupt membrane phase behavior (73, 74).

ACKNOWLEDGMENTS. We are grateful to Zvonimir Dogic and Prerna Sharma for generously suggesting ideas, sharing data, and critically reading our manuscript. We thank our reviewers for offering constructive suggestions. We acknowledge financial support from the National Science Foundation through Grant DMR-1104707. T.C.L. is grateful for support from a Simons Investigator grant.

- Dogic Z, Fraden S (2000) Cholesteric phase in virus suspensions. *Langmuir* 16(20): 7820–7824.
- Purdy KR, et al. (2003) Measuring the nematic order of suspensions of colloidal fd virus by x-ray diffraction and optical birefringence. *Phys Rev E Stat Nonlin Soft Matter Phys* 67(3 Pt 1):031708.
- Dogic Z, Purdy KR, Grelet E, Adams M, Fraden S (2004) Isotropic-nematic phase transition in suspensions of filamentous virus and the neutral polymer Dextran. *Phys Rev E Stat Nonlin Soft Matter Phys* 69(5):051702.
- Lettinga MP, Dogic Z, Wang H, Vermant J (2005) Flow behavior of colloidal rodlike viruses in the nematic phase. *Langmuir* 21(17):8048–8057.
- Dogic Z, Fraden S (2006) Ordered phases of filamentous viruses. *Curr Opin Colloid Interface Sci* 11(1):47–55.
- Tombolato F, Ferrarini A, Grelet E (2006) Chiral nematic phase of suspensions of rodlike viruses: Left-handed phase helicity from a right-handed molecular helix. *Phys Rev Lett* 96(25):258302.
- Barry E, Beller D, Dogic Z (2009) A model liquid crystalline system based on rodlike viruses with variable chirality and persistence length. *Soft Matter* 5(13):2563–2570.
- Barry E, Dogic Z, Meyer RB, Pelcovits RA, Oldenbourg R (2009) Direct measurement of the twist penetration length in a single smectic A layer of colloidal virus particles. *J Phys Chem B* 113(12):3910–3913.
- Pelcovits RA, Meyer RB (2009) Twist penetration in single-layer smectic A discs of colloidal virus particles. *Liq Cryst* 36(10–11):1157–1160.
- Barry E, Dogic Z (2010) Entropy driven self-assembly of nonamphiphilic colloidal membranes. *Proc Natl Acad Sci USA* 107(23):10348–10353.
- Kaplan CN, Tu H, Pelcovits RA, Meyer RB (2010) Theory of depletion-induced phase transition from chiral smectic-A twisted ribbons to semi-infinite flat membranes. *Phys Rev E Stat Nonlin Soft Matter Phys* 82(2 Pt 1):021701.
- Yang Y, Barry E, Dogic Z, Hagan MF (2012) Self-assembly of 2D membranes from mixtures of hard rods and depleting polymers. *Soft Matter* 8(3): 707–714.
- Gibaud T, et al. (2012) Reconfigurable self-assembly through chiral control of interfacial tension. *Nature* 481(7381):348–351.
- Tu H, Pelcovits RA (2013) Theory of self-assembled smectic-A crenellated disks: Membranes with cusped edges. *Phys Rev E* 87(3):032504.
- Tu H, Pelcovits RA (2013) Instability of flat disks with respect to the formation of twisted ribbons in smectic-A monolayers. *Phys Rev E Stat Nonlin Soft Matter Phys* 87(4):042505.
- Kaplan CN, Meyer RB (2014) Colloidal membranes of hard rods: Unified theory of free edge structure and twist walls. *Soft Matter* 10(26):4700–4710.
- Zakhary MJ, et al. (2014) Imprintable membranes from incomplete chiral coalescence. *Nat Commun* 5:3063.
- Sharma P, Ward A, Gibaud T, Hagan MF, Dogic Z (2014) Hierarchical organization of chiral rafts in colloidal membranes. *Nature* 513(7516):77–80.
- Kang L, Gibaud T, Dogic Z, Lubensky TC (2016) Entropic forces stabilize diverse emergent structures in colloidal membranes. *Soft Matter* 12(2):386–401.
- Asakura S, Oosawa F (1954) On interaction between two bodies immersed in a solution of macromolecules. *J Chem Phys* 22:1255–1256.
- Asakura S, Oosawa F (1958) Interaction between particles suspended in solutions of macromolecules. *J Polymer Sci* 33(126):183–192.

22. Lau AWC, Prasad A, Dogic Z (2009) Condensation of isolated semi-flexible filaments driven by depletion interactions. *Europhys Lett* 87(4):48006.
23. Ioan CE, Aberle T, Burchard W (2000) Structure properties of dextran. 2. Dilute solution. *Macromolecules* 33(15):5730–5739.
24. Armstrong JK, Wenby RB, Meiselman HJ, Fisher TC (2004) The hydrodynamic radii of macromolecules and their effect on red blood cell aggregation. *Biophys J* 87(6):4259–4270.
25. Banks DS, Fradin C (2005) Anomalous diffusion of proteins due to molecular crowding. *Biophys J* 89(5):2960–2971.
26. Harnau L, Dietrich S (2007) Inhomogeneous platelets and rod fluids. *Soft Matter*, eds. Gompper G, Schick M. (Wiley-VCH, Weinheim, Germany), Vol 3, pp 156–311.
27. Gast AP, Hall CK, Russel WB (1983) Polymer-induced phase separations in nonaqueous colloidal suspensions. *J Colloid Interface Sci* 96(1):251–267.
28. Gasser U, Weeks ER, Schofield A, Pusey PN, Weitz DA (2001) Real-space imaging of nucleation and growth in colloidal crystallization. *Science* 292(5515):258–262.
29. Pusey PN, van Megen W (1986) Phase behaviour of concentrated suspensions of nearly hard colloidal spheres. *Nature* 320(6060):340–342.
30. Weeks ER, Crocker JC, Levitt AC, Schofield A, Weitz DA (2000) Three-dimensional direct imaging of structural relaxation near the colloidal glass transition. *Science* 287(5453):627–631.
31. Lekkerkerker HNW, Poon WC-K, Pusey PN, Stroobants A, Warren PB (1992) Phase behaviour of colloid + polymer mixtures. *Europhys Lett* 20(6):559–564.
32. Aarts DGAL, Schmidt M, Lekkerkerker HNW (2004) Direct visual observation of thermal capillary waves. *Science* 304(5672):847–850.
33. Aarts DGAL, Dullens RPA, Lekkerkerker HNW, Bonn D, van Roij R (2004) Interfacial tension and wetting in colloid-polymer mixtures. *J Chem Phys* 120(4):1973–1980.
34. Lekkerkerker HNW, van der Kooij FM, Kassapidou K (2000) Liquid crystal phase transitions in suspensions of polydisperse plate-like particles. *Nature* 406(6798):868–871.
35. Lettinga MP, Gilet E (2007) Self-diffusion of rodlike viruses through smectic layers. *Phys Rev Lett* 99(19):197802.
36. Dietrich C, et al. (2001) Lipid rafts reconstituted in model membranes. *Biophys J* 80(3):1417–1428.
37. Veatch SL, Keller SL (2003) Separation of liquid phases in giant vesicles of ternary mixtures of phospholipids and cholesterol. *Biophys J* 85(5):3074–3083.
38. Lingwood D, Simons K (2009) Lipid rafts as a membrane-organizing principle. *Science* 327(5961):46–50.
39. Xie S, Hagan MF, Pelcovits RA (2016) Interaction of chiral rafts in self-assembled colloidal membranes. *Phys Rev E* 93(3):032706.
40. Sakhardande R, et al. (2016) Theory of microphase separation in bidisperse chiral membranes. arXiv:1604.03012.
41. Allendoerfer CB (1948) Steiner's formulae on a general S^{n+1} . *Bull New Ser Am Math Soc* 54(2):128–135.
42. Hansen-Goos H, Roth R, Mecke K, Dietrich S (2007) Solvation of proteins: Linking thermodynamics to geometry. *Phys Rev Lett* 99(12):128101.
43. Chaikin PM, Lubensky TC (1995) *Principles of Condensed Matter Physics* (Cambridge Univ Press, Cambridge, UK), pp 601–620.
44. Slater JC (1937) Wave functions in a periodic potential. *Phys Rev* 51:846–851.
45. Frank FC (1958) I. Liquid crystals. On the theory of liquid crystals. *Discuss Faraday Soc* 25:19–28.
46. Bak P (1982) Commensurate phases, incommensurate phases and the devil's staircase. *Rep Progr Phys* 45(6):587–629.
47. Born M, Wolf E (2005) *Principles of Optics* (Cambridge Univ Press, Cambridge, UK), 7th Ed.
48. Hinshaw GA, Jr, Petschek RG, Pelcovits RA (1988) Modulated phases in thin ferroelectric liquid-crystal films. *Phys Rev Lett* 60(18):1864–1867.
49. Hinshaw GA, Jr, Petschek RG (1989) Transitions and modulated phases in chiral tilted smectic liquid crystals. *Phys Rev A Gen Phys* 39(11):5914–5926.
50. Selinger JV, Wang ZG, Bruinsma RF, Knobler CM (1993) Chiral symmetry breaking in Langmuir monolayers and smectic films. *Phys Rev Lett* 70(8):1139–1142.
51. Samsonov AV, Mihalyov I, Cohen FS (2001) Characterization of cholesterol-sphingomyelin domains and their dynamics in bilayer membranes. *Biophys J* 81(3):1486–1500.
52. Kuzmin PI, Akimov SA, Chizmadzhev YA, Zimmerberg J, Cohen FS (2005) Line tension and interaction energies of membrane rafts calculated from lipid splay and tilt. *Biophys J* 88(2):1120–1133.
53. Katsaras J, Gutberlet T (2013) *Lipid Bilayers: Structure and Interactions, Biological and Medical Physics, Biomedical Engineering* (Springer, Berlin), pp 30–34.
54. Tardieu A, Luzzati V, Reman FC (1973) Structure and polymorphism of the hydrocarbon chains of lipids: A study of lecithin-water phases. *J Mol Biol* 75(4):711–733.
55. Simons K, Ikonen E (1997) Functional rafts in cell membranes. *Nature* 387(6633):569–572.
56. Alberts B, et al. (2015) *Molecular Biology of the Cell* (Garland Science, New York), 6th Ed, pp 572–574.
57. Reintzer F (1888) Beiträge zur Kenntniss des Cholesterins [Contributions to the knowledge of cholesterol]. *Monatsh Chem* 9(1):421–441. German.
58. Seul M, Morgan NY, Sire C (1994) Domain coarsening in a two-dimensional binary mixture: Growth dynamics and spatial correlations. *Phys Rev Lett* 73(17):2284–2287.
59. Anderson RGW, Jacobson K (2002) A role for lipid shells in targeting proteins to caveolae, rafts, and other lipid domains. *Science* 296(5574):1821–1825.
60. Cluzeau P, Joly G, Nguyen HT, Dolganov VK (2002) Two-dimensional ordering of inclusions in smectic-C films. *Pis'ma v Zh Eksp Teoret Fiz* 75(9):482–486.
61. Bohley C, Stannarius R (2008) Inclusions in free standing smectic liquid crystal films. *Soft Matter* 4(4):683.
62. Silvestre NM, et al. (2009) Modeling dipolar and quadrupolar defect structures generated by chiral islands in freely suspended liquid crystal films. *Phys Rev E Stat Nonlin Soft Matter Phys* 80(4):041708.
63. Constantin D, Brotons G, Jarre A, Li C, Salditt T (2007) Interaction of alamethicin pores in DMPC bilayers. *Biophys J* 92(11):3978–3987.
64. Constantin D (2009) Membrane-mediated repulsion between gramicidin pores. *Biochim Biophys Acta* 1788(9):1782–1789.
65. Ramstedt B, Slotte JP (1999) Comparison of the biophysical properties of racemic and d-erythro-N-acyl sphingomyelins. *Biophys J* 77(3):1498–1506.
66. Lalitha S, Sampath Kumar A, Stine KJ, Covey DF (2001) Chirality in membranes: First evidence that enantioselective interactions between cholesterol and cell membrane lipids can be a determinant of membrane physical properties. *J Supramol Chem* 1(2):53–61.
67. Lalitha S, Kumar AS, Covey DF, Stine KJ (2001) Enantiospecificity of sterol-lipid interactions: First evidence that the absolute configuration of cholesterol affects the physical properties of cholesterol-sphingomyelin membranes. *Chem Commun* (13):1192–1193.
68. Westover EJ, Covey DF, Brockman HL, Brown RE, Pike LJ (2003) Cholesterol depletion results in site-specific increases in epidermal growth factor receptor phosphorylation due to membrane level effects: Studies with cholesterol enantiomers. *J Biol Chem* 278(51):51125–51133.
69. Westover EJ, Covey DF (2004) The enantiomer of cholesterol. *J Membr Biol* 202(2):61–72.
70. Lysko GS, Robinson JL, Casto R, Ferrone RA (1994) The stereospecific effects of isoflurane isomers in vivo. *Eur J Pharmacol* 263(1–2):25–29.
71. Dickinson R, White I, Lieb WR, Franks NP (2000) Stereoselective loss of righting reflex in rats by isoflurane. *Anesthesiology* 93(3):837–843.
72. Won A, et al. (2006) Chirality in anesthesia I: Minimum alveolar concentration of secondary alcohol enantiomers. *Anesth Analg* 103(1):81–84.
73. Campagna JA, Miller KW, Forman SA (2003) Mechanisms of actions of inhaled anesthetics. *N Engl J Med* 348(21):2110–2124.
74. Weinrich M, et al. (2012) Halothane changes the domain structure of a binary lipid membrane. *Langmuir* 28(10):4723–4728.

Supporting Information

Supporting Information Corrected xxx xx, xxxx

Kang et al. 10.1073/pnas.1613732114

Derivation of the Single-Domain Free Energy

We must be careful to maintain volume conservation in this system, so let us conceptualize the raft formation process in two stages. First, the untwisted two-component membrane of radius R_t with raft area fraction α^2 is divided into untwisted tiling domains of radius R , each of which contains a raft of radius αR (Fig. 3B of main text). Second, the rods in each domain twist with angle $\theta(r) \ll 1$ (Fig. 3C). Doing so, however, decreases the thickness of the membrane slightly, so to conserve volume in both the raft and the background, each domain has to grow slightly from radius R to R' and its raft must grow slightly from radius αR to $\alpha' R'$. Mathematically, volume conservation for the raft and the background appears respectively as

$$\int_0^{\alpha' R'} dr r l_1 \cos \theta = \int_0^{\alpha R} dr r l_1, \quad [S1]$$

$$\int_0^{R'} dr r l_2 \cos \theta = \int_0^R dr r l_2.$$

If we expand to quadratic order in $\theta(r)$, we get

$$\int_0^{\alpha' R'} dr r = \int_0^{\alpha R} dr r + \frac{1}{2} \int_0^{\alpha' R'} dr r \theta^2, \quad [S2]$$

$$\int_0^{R'} dr r = \int_0^R dr r + \frac{1}{2} \int_0^{R'} dr r \theta^2.$$

Thus, the projected areas in the x - y plane of the raft and the background increase by terms proportional to θ^2 due to rod twist and volume conservation (Fig. 3E).

The free energies of the raft and the background are each described by the single-component membrane free energies F_{dep} and F_{Frank} (Eqs. 1 and 7 of the main text). In addition, the change in membrane half thickness by $d \cos \theta_0$ at the raft-background interface creates extra excluded volume, which leads to an interfacial line tension (Fig. 3D). The combination of these effects, to quadratic order in θ and the virus half-length difference d , gives

$$\frac{F_{\text{domain}}}{4\pi caT} = d\alpha' R' + \int_0^{\alpha' R'} dr \left[r + \frac{\lambda_1^2}{2} (r(\partial_r \theta)^2 + 2\theta \partial_r \theta) + \frac{\theta^2}{r} - 2q_1 r \partial_r \theta - 2q_1 \theta \right] + \int_0^{R'} dr \left[r + \frac{\lambda_2^2}{2} (r(\partial_r \theta)^2 + 2\theta \partial_r \theta + \frac{\theta^2}{r} - 2q_2 r \partial_r \theta - 2q_2 \theta) \right]. \quad [S3]$$

$\lambda_j = \sqrt{K_j l_j / caT}$ is the twist penetration depth, where $j \in \{1, 2\}$ corresponds to raft and background, respectively. Actually, only the twist mode contributes to this free energy to quadratic order in θ , so the single Frank elastic constant K_j reflects only the twist elastic constant in this equation and does not correspond to the splay or bend elastic constants.

Using $2\theta \partial_r \theta = \partial_r(\theta^2)$, $r \partial_r \theta + \theta = \partial_r(r\theta)$, and Eq. S2, the domain free energy becomes

$$\frac{F_{\text{domain}}}{4\pi caT} = \frac{1}{2} R^2 + d\alpha' R' - [\lambda_1^2 q_1 - \lambda_2^2 q_2] \alpha' R' \theta_0 + \frac{1}{2} [\lambda_1^2 - \lambda_2^2] \theta_0^2$$

$$+ \int_0^{\alpha' R'} dr \left[\frac{1}{2} r \theta^2 + \frac{\lambda_1^2}{2} \left(r(\partial_r \theta)^2 + \frac{\theta^2}{r} \right) \right] + \int_0^{R'} dr \left[\frac{1}{2} r \theta^2 + \frac{\lambda_2^2}{2} \left(r(\partial_r \theta)^2 + \frac{\theta^2}{r} \right) \right]. \quad [S4]$$

Every term with $\alpha' R'$ and R' is either linear or quadratic in d and θ , so to quadratic order, we can use αR and R instead:

$$\frac{F_{\text{domain}}}{4\pi caT} = \frac{1}{2} R^2 + d\alpha R - [\lambda_1^2 q_1 - \lambda_2^2 q_2] \alpha R \theta_0 + \frac{1}{2} [\lambda_1^2 - \lambda_2^2] \theta_0^2 + \int_0^{\alpha R} dr \left[\frac{1}{2} r \theta^2 + \frac{\lambda_1^2}{2} \left(r(\partial_r \theta)^2 + \frac{\theta^2}{r} \right) \right] + \int_0^R dr \left[\frac{1}{2} r \theta^2 + \frac{\lambda_2^2}{2} \left(r(\partial_r \theta)^2 + \frac{\theta^2}{r} \right) \right]. \quad [S5]$$

To be precise, the radii αR and R indicated in Fig. 3 of the main text should actually be their primed counterparts, but this correction is quadratic in θ and thus small. Multiplying Eq. S5 by the number of rafts R_t^2/R^2 gives the membrane structure free energy Eq. 9 of the main text, ignoring a constant term proportional to R_t^2 .

Calculation of the Virus Tilt Angle

From the membrane structure free energy Eq. 9 of the main text, we can calculate the virus tilt angle $\theta(r)$ by solving its Euler-Lagrange equations. We first focus on the raft domain and rewrite its integral in a dimensionless manner with the substitutions $s_1 = r/\lambda_1$ and $S_1 = R/\lambda_1$,

$$\int_0^{\alpha R} dr \left[\frac{1}{2} r \theta^2 + \frac{\lambda_1^2}{2} \left(r(\partial_r \theta)^2 + \frac{\theta^2}{r} \right) \right] = \frac{\lambda_1^2}{2} \int_0^{\alpha S_1} ds_1 \left[s_1 \theta^2 + \frac{\theta^2}{s_1} + s_1 (\partial_{s_1} \theta)^2 \right] = \frac{\lambda_1^2}{2} \int_0^{\alpha S_1} ds_1 [s_1 \theta \partial_{s_1}^2 \theta + \theta \partial_{s_1} \theta + s_1 (\partial_{s_1} \theta)^2] = \frac{\lambda_1^2}{2} (s_1 \theta \partial_{s_1} \theta) \Big|_{s_1=0}^{\alpha S_1}, \quad [S6]$$

where the last two expressions were obtained through the Euler-Lagrange equation

$$s_1^2 \partial_{s_1}^2 \theta + s_1 \partial_{s_1} \theta - (s_1^2 + 1) \theta = 0, \quad [S7]$$

which is a Bessel differential equation. The boundary conditions for the raft are $\theta(0) = 0$ and $\theta(\alpha S_1) = \theta_0$. We can obtain the same equation for the background with the substitutions $s_2 = r/\lambda_2$ and $S_2 = R/\lambda_2$, and its boundary conditions are $\theta(\alpha S_2) = \theta_0$ and $\theta(S_2) = 0$. Solving for $\theta(r)$ gives Eq. 11 of the main text.

Calculation of the Raft Shift Free Energy

The shifted polar coordinates used to calculate the raft shift free energy are

$$x = r \cos \phi + b(r) \quad \text{and} \quad y = r \sin \phi. \quad [S8]$$

We calculate Eq. 18 of the main text explicitly by substituting in expressions for the scale factors

$$h_r = \sqrt{(\partial_r x)^2 + (\partial_r y)^2} = \sqrt{1 + 2\partial_r b \cos \phi + (\partial_r b)^2} \quad [S9]$$

$$h_\phi = \sqrt{(\partial_\phi x)^2 + (\partial_\phi y)^2} = r$$

and the nematic director

$$\mathbf{n}(r, \phi) = \sin \psi(r, \phi) \sin \theta(r, \phi) \hat{\mathbf{r}} - \cos \psi(r, \phi) \sin \theta(r, \phi) \hat{\phi} + \cos \theta(r, \phi) \hat{\mathbf{z}}. \quad [\text{S10}]$$

$\theta(r, \phi) = \theta(r) + \vartheta(r) \cos \phi$, where θ and ϑ are the monopolar and dipolar components of the tilt angle. The angle $\psi(r, \phi) = \psi(r) \sin \phi$, also to dipolar order, rotates the tilt axis of the particles to produce an $\hat{\mathbf{r}}$ component in \mathbf{n} . The result, to quadratic order in the angles, is

$$\begin{aligned} \frac{F_{\text{shift}}}{2caT} = & \int_{\alpha R}^R dr \int_0^{2\pi} d\phi \left\{ \frac{1}{2} r (\theta + \vartheta \cos \phi)^2 \right. \\ & \times \sqrt{1 + 2\partial_r b \cos \phi + (\partial_r b)^2} \\ & + \frac{\lambda_2^2}{2} \frac{(r\partial_r \theta + r\partial_r \vartheta \cos \phi + \theta + \vartheta \cos \phi)^2}{r \sqrt{1 + 2\partial_r b \cos \phi + (\partial_r b)^2}} \\ & \left. + \frac{\lambda_2^2}{2} \frac{[\theta\partial_r b + \vartheta + 3\vartheta\partial_r b \cos \phi + \vartheta(\partial_r b)^2]^2 \sin^2 \phi}{r [1 + 2\partial_r b \cos \phi + (\partial_r b)^2]^{3/2}} \right\}. \quad [\text{S11}] \end{aligned}$$

Note that ψ does not appear, so we set $\psi = 0$. The shifted coordinate system introduces splay deformations into this quadratic-order free energy, so the single Frank elastic constant describes the energetic cost of both twist and splay deformations. We can perform the integral over ϕ to obtain the complicated expression

$$\begin{aligned} \frac{F_{\text{shift}}}{2caT} = & \int_{\alpha R}^R \frac{dr}{r} \left\{ \frac{1}{1 + \partial_r b} k[\theta, \vartheta, b; r] K \left(\frac{2\sqrt{\partial_r b}}{1 + \partial_r b} \right) \right. \\ & \left. + (1 + \partial_r b) e[\theta, \vartheta, b; r] E \left(\frac{2\sqrt{\partial_r b}}{1 + \partial_r b} \right) \right\}, \quad [\text{S12}] \end{aligned}$$

where K and E are complete elliptic integrals of the first and second kinds, respectively, and

$$\begin{aligned} k[\theta, \vartheta, b; r] = & \lambda_2^2 \theta^2 [1 + (\partial_r b)^2] + 2\lambda_2^2 (\theta + r\partial_r \theta)^2 \\ & - 2\lambda_2^2 (\theta + r\partial_r \theta) (\vartheta + r\partial_r \vartheta) [1 + (\partial_r b)^2] \\ & + \frac{4}{3} (2r^2 + 3\lambda_2^2) \theta \partial_r \vartheta b - \frac{2}{3} (r^2 + \lambda_2^2) \\ & \times \frac{\theta \vartheta [1 + (\partial_r b)^2]}{\partial_r b} - \frac{1}{5} (2r^2 + 13\lambda_2^2) \vartheta^2 [1 + (\partial_r b)^2] \\ & + \frac{1}{15} (r^2 + 9\lambda_2^2) \frac{\vartheta^2 [1 + (\partial_r b)^2] [1 + 4(\partial_r b)^2 + (\partial_r b)^4]}{(\partial_r b)^2} \\ & + \frac{1}{3} \lambda_2^2 \frac{(\vartheta + r\partial_r \vartheta)^2 [1 + 4(\partial_r b)^2 + (\partial_r b)^4]}{(\partial_r b)^2}, \quad [\text{S13}] \end{aligned}$$

$$\begin{aligned} e[\theta, \vartheta, b; r] = & (2r^2 - \lambda_2^2) \theta^2 + \frac{2}{3} (r^2 + 3\lambda_2^2) \frac{\theta \vartheta [1 + (\partial_r b)^2]}{\partial_r b} \\ & + 2\lambda_2^2 \frac{(\theta + r\partial_r \theta) (\vartheta + r\partial_r \vartheta)}{\partial_r b} \\ & + \frac{1}{3} (4r^2 + 9\lambda_2^2) \vartheta^2 \\ & - \frac{1}{15} (r^2 + 9\lambda_2^2) \frac{\vartheta^2 [1 + 4(\partial_r b)^2 + (\partial_r b)^4]}{(\partial_r b)^2} \\ & - \frac{1}{3} \lambda_2^2 \frac{(\vartheta + r\partial_r \vartheta)^2 [1 + (\partial_r b)^2]}{(\partial_r b)^2}. \quad [\text{S14}] \end{aligned}$$

We can simplify the shift energy Eq. S12 in the limit of small raft shifts with $\partial_r b \ll 1$. Assuming small deformations, we expect that θ retains its unshifted profile (Eq. 11 of the main text). We can directly calculate ΔF_{shift} , which is F_{shift} minus the unshifted

free energy of the domain in which $b = 0$. To quadratic order in $\partial_r b$,

$$\begin{aligned} \frac{\Delta F_{\text{shift}}}{4\pi caT} = & \int_{\alpha R}^R dr \left\{ \frac{1}{8} [2r\vartheta^2 + r\theta^2 (\partial_r b)^2] \right. \\ & + \frac{\lambda_2^2}{8} [2r(\partial_r \vartheta)^2 + 4\vartheta\partial_r \vartheta + 4\frac{\vartheta^2}{r} \\ & \left. + \left(r(\partial_r \theta)^2 + 2\theta\partial_r \theta + 3\frac{\theta^2}{r} \right) (\partial_r b)^2 \right\}. \quad [\text{S15}] \end{aligned}$$

First, note that ϑ and b are uncoupled. The terms corresponding to ϑ can be written as a sum of squares, so $\vartheta = 0$. Thus,

$$\frac{\Delta F_{\text{shift}}}{4\pi caT} = \int_{\alpha R}^R dr \left[\frac{1}{8} r \theta^2 + \frac{\lambda_2^2}{8} \left(r(\partial_r \theta)^2 + 2\theta\partial_r \theta + 3\frac{\theta^2}{r} \right) (\partial_r b)^2 \right] \quad [\text{S16}]$$

In the large radius limit where $\alpha R \gg \lambda_2$, we can make numerous simplifications, including

$$\theta(r) \sim \theta_0 \sqrt{\frac{\alpha R}{r}} \frac{\sinh[(R-r)/\lambda_2]}{\sinh[(R-\alpha R)/\lambda_2]}. \quad [\text{S17}]$$

This transforms Eq. S16 to

$$\begin{aligned} \frac{\Delta F_{\text{shift}}}{4\pi caT} = & \frac{\alpha R}{8} \text{csch}^2[(R-\alpha R)/\lambda_2] \theta_0^2 \\ & \times \int_{\alpha R}^R dr \cosh[2(R-r)/\lambda_2] (\partial_r b)^2. \quad [\text{S18}] \end{aligned}$$

The Euler-Lagrange equation for $b(r)$ can be integrated to give

$$b(r) \approx b_0 \frac{\arctan \tanh[(R-r)/\lambda_2]}{\arctan \tanh[(R-\alpha R)/\lambda_2]}. \quad [\text{S19}]$$

Substituting this into Eq. S18 yields the energy

$$\frac{\Delta F_{\text{shift}}}{4\pi caT} \approx \frac{\alpha R}{8\lambda_2} \frac{\text{csch}^2[(R-\alpha R)/\lambda_2]}{\arctan \tanh[(R-\alpha R)/\lambda_2]} \theta_0^2 b_0^2. \quad [\text{S20}]$$

Landau Coefficients for Phase Separation

In the main text, we argued that mixing preferentially occurs in the background phase and can be ignored in the raft phase because a long rod among a sea of short ones contributes much more extra excluded volume than a short rod among a sea of long ones (Fig. 2C of the main text). However, if we imagine decreasing the difference in virus half-lengths d to a very small value, excluded volume differences should be severely reduced and mixing should occur in both phases. Here, we explore the onset of phase separation and asymmetric mixing properties in the limit $d \ll \xi/2 \ll a$, where ξ is the virus-virus separation and a is the depletant radius. Note that the first inequality is not compatible with the experimental values $d = 130$ nm and $\xi = 12$ nm used in the main text.

The membrane can be described by an Ising-like model in this limit. We assume a hexagonal lattice with lattice constant ξ whose sites are occupied with either a long L virus or a short S virus. L viruses naturally contribute more excluded volume— $\sqrt{3}\xi^2 d$ per particle—than do the S viruses. However, because of the effect of surface convexity on excluded volume, an L particle will contribute an even greater amount of excluded volume when it is adjacent to an S particle (Fig. S14)—approximately $ad^2/\sqrt{3}$ per L - S pair. And because this extra excluded volume lies closer to the S virus in each heterogeneous pair, a symmetry between L and S viruses is broken, and three-particle couplings are permitted. Indeed, as depicted in Fig. S1B, there are even smaller amounts of additional and reduced excluded volume for L - S - S and L - L - S nearest-neighbor triplets, respectively—approximately $\pm \pi a^2 d^3/9\xi^2$ per triplet. Using Eq. 1 of the main text, we can write these excluded volume effects in terms of

a depletion free energy. We use $\phi_i^L \in \{0, 1\}$ to indicate the absence and presence, respectively, of an L particle at lattice site i ; and $\phi_i^S = 1 - \phi_i^L$ acts similarly as an indicator for S viruses. The effective Ising-like Hamiltonian is

$$\begin{aligned} \frac{H}{Tc} = & \sqrt{3}\xi^2 d \sum_i \phi_i^L + \frac{1}{\sqrt{3}}ad^2 \sum_{\langle ij \rangle} (\phi_i^L \phi_j^S + \phi_i^S \phi_j^L) \\ & + \frac{\pi}{9} \frac{a^2 d^3}{\xi^2} \sum_{\langle ijk \rangle} [(\phi_i^L \phi_j^S \phi_k^S + \phi_i^S \phi_j^L \phi_k^S + \phi_i^S \phi_j^S \phi_k^L) \\ & - (\phi_i^L \phi_j^L \phi_k^S + \phi_i^L \phi_j^S \phi_k^L + \phi_i^S \phi_j^L \phi_k^L)], \end{aligned} \quad [\text{S21}]$$

where $\langle ij \rangle$ indicates nearest-neighbor pairs of lattice sites and $\langle ijk \rangle$ indicates nearest-neighbor triplets of lattice sites. c is depletant concentration and T is temperature. We convert the ϕ s to the symmetric order parameter $\psi_i = \pm 1$, where positive (negative) corresponds to an L (S) virus at site i . Thus,

$$\phi_i^L = \frac{1 + \psi_i}{2} \quad \text{and} \quad \phi_i^S = \frac{1 - \psi_i}{2}. \quad [\text{S22}]$$

This converts Eq. S21 to

$$\begin{aligned} \frac{H}{Tc} = & \frac{\sqrt{3}}{2} \xi^2 d \sum_i \psi_i - \frac{1}{2\sqrt{3}} ad^2 \sum_{\langle ij \rangle} \psi_i \psi_j \\ & + \frac{\pi}{12} \frac{a^2 d^3}{\xi^2} \sum_{\langle ijk \rangle} \psi_i \psi_j \psi_k, \end{aligned} \quad [\text{S23}]$$

to leading orders in d and ignoring constant terms.

The first term acts as a chemical potential that would favor $\psi_i = -1$; for our system, we assume that the membrane, once formed, maintains fixed numbers of L and S viruses. Thus, $\sum_i \psi_i$ is conserved and we ignore the linear term. We now take mean-field and continuum limits. For the quadratic term, we allow slow variations in the mean-field order parameter $\psi(x, y) \equiv \langle \psi_i \rangle$, which reflects the local concentration difference between the two virus species, with

$$\begin{aligned} \sum_{\langle ij \rangle} \psi_i \psi_j & \rightarrow c_v \int dx dy \psi(x, y) \left[\psi(x - \xi, y) \right. \\ & \quad \left. + \psi\left(x + \frac{\xi}{2}, y + \frac{\sqrt{3}\xi}{2}\right) + \psi\left(x + \frac{\xi}{2}, y - \frac{\sqrt{3}\xi}{2}\right) \right] \\ & = c_v \int dx dy \left[3\psi(x, y)^2 \right. \\ & \quad \left. + \frac{3}{4}\xi^2 \psi(x, y)(\partial_x^2 + \partial_y^2)\psi(x, y) \right] \\ & = c_v \int d^2 \mathbf{x} \left[3\psi^2 - \frac{3}{4}\xi^2 (\nabla \psi)^2 \right], \end{aligned} \quad [\text{S24}]$$

where we have integrated by parts and ignored boundary terms. $c_v = 2/\sqrt{3}\xi^2$ is the 2D virus concentration. For the cubic term, we note that there are twice as many nearest-neighbor triplets as lattice points to obtain

$$\sum_{\langle ijk \rangle} \psi_i \psi_j \psi_k \rightarrow 2c_v \int d^2 \mathbf{x} \psi^3. \quad [\text{S25}]$$

The mean-field Hamiltonian is thus (without the linear term)

$$\frac{\langle H \rangle}{c_v T} = cad^2 \int d^2 \mathbf{x} \left[-\frac{\sqrt{3}}{2} \psi^2 + \frac{\pi}{6} \frac{ad}{\xi^2} \psi^3 + \frac{\sqrt{3}}{8} \xi^2 (\nabla \psi)^2 \right]. \quad [\text{S26}]$$

Meanwhile, the entropy of mixing follows in analogy to Eq. 3 of the main text with the substitutions in Eq. S22:

$$\frac{S_{\text{mix}}}{c_v} = \int d^2 \mathbf{x} \left[\frac{1 - \psi}{2} \log \frac{1 - \psi}{2} + \frac{1 + \psi}{2} \log \frac{1 + \psi}{2} \right]. \quad [\text{S27}]$$

Thus, the free energy to leading orders in ψ is

$$\begin{aligned} \frac{F_{\text{Landau}}}{c_v T} = & \frac{\langle H \rangle - TS_{\text{mix}}}{c_v T} = \int d^2 \mathbf{x} \left[\left(\frac{1}{2} - \frac{\sqrt{3}}{2} cad^2 \right) \psi^2 \right. \\ & \left. + \frac{\pi}{6} \frac{ca^2 d^3}{\xi^2} \psi^3 + \frac{1}{12} \psi^4 + \frac{\sqrt{3}}{8} cad^2 \xi^2 (\nabla \psi)^2 \right]. \end{aligned} \quad [\text{S28}]$$

This expression provides values for the coefficients of a phenomenological Landau expansion in ψ , such as that used in ref. 40 of the main text. It illustrates the equivalence between our system and liquid-gas phase separation, with a critical point at $c = 1/\sqrt{3}ad^2$. Around this point, $cad^2 \sim 1$, so the characteristic domain wall width between regions of different ψ s is the interparticle distance $\sim \xi$. When c exceeds this critical value, the free energy Eq. S28 has both positive and negative local minima

$$\psi_{\pm} = \pm \sqrt{\frac{1}{\sqrt{3}} cad^2 - \frac{1}{3}} - \frac{\pi}{12} \frac{ca^2 d^3}{\xi^2} \quad [\text{S29}]$$

to leading orders in d . Note that the cubic term, which arises from asymmetric effects of depletion on long vs. short particles, makes ψ_+ less positive and ψ_- more negative, indicating that mixing is enhanced in the L -rich phase and hindered in the S -rich phase. As d increases, these effects grow until the S -rich phase can be considered completely pure and all mixing occurs in the L -rich phase, a regime demonstrated by the raft and background phases of fd and M13 viruses in the main text.

Chiral Contribution to Phase Separation

With the parameter values given in Table 1 of the main text, numerical minimization of the total free energy combining bare phase separation (Eq. 4) and raft structure (Eq. 13) over α and R yields results indistinguishable from sequential minimization of Eq. 4 over α and Eq. 13 over R . However, after multiplying both chiral wavenumbers q_{fd} and q_{M13} by various factors, combined minimization and sequential minimization produce different results (Fig. S2). Note that Eq. 4 does not depend on Δq and the Frank constant K , whereas Eq. 13 does. Thus, increasing the magnitude of the chiral wavenumber difference Δq places the system in a regime where the chiral membrane structure influences the degree of phase separation. A larger $|\Delta q|$ leads to a larger α , facilitating phase separation.

We can see this effect of Δq on α analytically in the $R \rightarrow \infty$ limit, where Eq. 13 becomes Eq. 14 of the main text. We introduce a small correction $\Delta\alpha$ that the structural free energy imposes on the α preferred by the phase separation free energy (Eq. 5 of the main text):

$$\alpha = \sqrt{\frac{\alpha_t^2 - e^{-2cd/c_v}}{1 - e^{-2cd/c_v}}} + \Delta\alpha. \quad [\text{S30}]$$

We then expand the combined free energy (Eq. 4 plus Eq. 14) to leading orders in $\Delta\alpha$ and $1/R$:

$$\begin{aligned} \frac{F_{\text{sep}} + F_{\text{struct}}}{\pi R_t^2 T} = & \frac{F_{\text{sep}}^0 + F_{\text{struct}}^0}{\pi R_t^2 T} + 4c \frac{a}{R} \left(d - \frac{1}{4} \lambda^3 \Delta q^2 \right) \Delta\alpha \\ & + c_v \frac{(\alpha_t^2 - e^{-2cd/c_v})(1 - e^{-2cd/c_v})}{(1 - \alpha_t^2)e^{-2cd/c_v}} \Delta\alpha^2. \end{aligned} \quad [\text{S31}]$$

Here, the 0 superscript indicates the unperturbed free energies that do not depend on $\Delta\alpha$. The coefficient of the quadratic term is always positive when $\alpha \neq 0$. The coefficient of the linear term includes an overall factor of a/R and is thus small for large R . When it is positive, the membrane is in the regime of a single large raft, so $R \rightarrow \infty$ and the linear term vanishes. The membrane thus prefers $\Delta\alpha = 0$, and the structure of the membrane does not affect phase separation. The coefficient of the linear term changes sign at the transition from a single large raft to multiple smaller rafts, becoming negative in the

latter regime and favoring a positive $\Delta\alpha$. Thus, we directly see in this limit that F_{sep} dominates the behavior of α and that chirality facilitates phase separation, because a larger $|\Delta q|$ favors a larger $\Delta\alpha$.

Overview of the Linear System

Here we present the major results of a rectangular membrane whose rafts are arranged as linear stripes of wavelength $2L$. Note that the same results can be obtained by taking the $R \rightarrow \infty$ limit of the circular raft system. The membrane has dimensions L_x and L_y , and the nematic director describing particle orientation is $\mathbf{n}(x) = -\sin\theta(x)\hat{\mathbf{y}} + \cos\theta(x)\hat{\mathbf{z}}$. The membrane free energy, in analogy to Eq. 9 of the main text, is

$$\frac{F_{\text{linear}}}{2caTL_y} = \frac{L_x}{L} \left\{ d - [\lambda_1^2 q_1 - \lambda_2^2 q_2] \theta_0 + \int_0^{\alpha L} dx \left[\frac{1}{2} \theta^2 + \frac{\lambda_1^2}{2} (\partial_x \theta)^2 \right] + \int_{\alpha L}^L dx \left[\frac{1}{2} \theta^2 + \frac{\lambda_2^2}{2} (\partial_x \theta)^2 \right] \right\}. \quad [\text{S32}]$$

The q s and λ s are defined identically to their definitions in the main text, with the raft phase extending from 0 to αL and the background phase from αL to L . The Euler-Lagrange equations for the raft and background phases are simply $\lambda_j^2 \partial_x^2 \theta - \theta = 0$, with $j \in \{1, 2\}$. The boundary conditions are $\theta(0) = 0$, $\theta(\alpha L) = \theta_0$, and $\theta(L) = 0$. Thus,

$$\theta(x) = \begin{cases} \theta_0 \frac{\sinh(x/\lambda_1)}{\sinh(\alpha L/\lambda_1)} & 0 \leq x \leq \alpha L \\ \theta_0 \frac{\sinh[(L-x)/\lambda_2]}{\sinh[(L-\alpha L)/\lambda_2]} & \alpha L \leq x \leq L. \end{cases} \quad [\text{S33}]$$

Substituting this into Eq. S32 yields

$$\frac{F_{\text{linear}}}{2caTL_y} = \frac{L_x}{L} \left\{ d - [\lambda_1^2 q_1 - \lambda_2^2 q_2] \theta_0 + \frac{1}{2} \left[\lambda_1 \coth(\alpha L/\lambda_1) + \lambda_2 \coth[(L-\alpha L)/\lambda_2] \right] \theta_0^2 \right\}. \quad [\text{S34}]$$

Thus,

$$\theta_0 = \frac{\lambda_1^2 q_1 - \lambda_2^2 q_2}{\lambda_1 \coth(\alpha L/\lambda_1) + \lambda_2 \coth[(L-\alpha L)/\lambda_2]}, \quad [\text{S35}]$$

leading to

$$\frac{F_{\text{linear}}}{2caTL_y} = \frac{L_x}{L} \left\{ d - \frac{1}{2} \frac{[\lambda_1^2 q_1 - \lambda_2^2 q_2]^2}{\lambda_1 \coth(\alpha L/\lambda_1) + \lambda_2 \coth[(L-\alpha L)/\lambda_2]} \right\} \quad [\text{S36}]$$

$$= \frac{L_x}{L} \left\{ d - \frac{1}{2} \frac{\lambda^3 \Delta q^2}{\coth(\alpha L/\lambda) + \coth[(L-\alpha L)/\lambda]} \right\}, \quad [\text{S37}]$$

under the assumption that $\lambda \equiv \lambda_1 = \lambda_2$, where $\Delta q = q_1 - q_2$.

In the limit where $L \rightarrow \infty$, this becomes

$$\frac{F_{\text{linear}}}{2caTL_y} \sim \frac{L_x}{L} \left\{ d - \frac{1}{4} \lambda^3 \Delta q^2 + \frac{1}{4} \lambda^3 \Delta q^2 \left[e^{-2\alpha L/\lambda} + e^{-2(1-\alpha)L/\lambda} \right] \right\}. \quad [\text{S38}]$$

Unlike the circularly symmetric case, there are no higher-order polynomial terms in L^{-1} . Thus, the transition to finite-sized striped rafts is directly analogous to the 1D Frenkel-Kontorova model at the commensurate-incommensurate transition.

We believe that the free-floating experimental system adopts a circular geometry due to the energy of the membrane edge, which, due to depletion, prefers rods to be tilted along the tangent to the edge. Perhaps a linear, striped configuration can be seen in very large or spherical membranes where edge effects are not important.

General Membrane Rafts Formed from Chiral Rod-Like Particles

Our theory easily generalizes to any membrane raft system that has three properties. First, the membrane particles are chiral and rod-like and thus prefer to twist at a particular wavenumber. This is described by the chiral Frank free energy presented as Eq. 7 of the main text, with single elastic constant K and chiral wavenumber q . Second, the particles prefer to align perpendicular to the membrane. This appears to lowest order as a harmonic free energy

$$F_{\text{align}} = \frac{D}{2} \int_C d^2 \mathbf{x} \theta^2. \quad [\text{S39}]$$

D is analogous to the smectic liquid crystal alignment parameter, but it multiplies an integral over 2D, not 3D, space. Third, a line tension exists at the interfaces between the two phases,

$$F_{\text{tension}} = \gamma \int_C ds, \quad [\text{S40}]$$

where the line integral travels along all interfaces C .

We approximate the rafts to tile the circular membrane of radius R_t via circular domains of radius R_j , just as in Fig. 3 of the main text. We take the raft area fraction α^2 to be an experimental parameter, although for certain systems, it may be possible to determine α from more fundamental physical principles, in analogy to the entropically derived Eq. 4. The structural free energy of this generalized system is

$$\begin{aligned} \frac{F_{\text{gen}}}{2\pi} = & \frac{R_t^2}{R^2} \left\{ \gamma \alpha R - [K_1 t_1 q_1 - K_2 t_2 q_2] \alpha R \theta_0 \right. \\ & + \frac{1}{2} [K_1 t_1 - K_2 t_2] \theta_0^2 \\ & + \int_0^{\alpha R} dr \left[\frac{D_1}{2} r \theta^2 + \frac{K_1 t_1}{2} \left(r (\partial_r \theta)^2 + \frac{\theta^2}{r} \right) \right] \\ & \left. + \int_{\alpha R}^R dr \left[\frac{D_2}{2} r \theta^2 + \frac{K_2 t_2}{2} \left(r (\partial_r \theta)^2 + \frac{\theta^2}{r} \right) \right] \right\}. \quad [\text{S41}] \end{aligned}$$

t is the thickness of the membrane, and the subscripts 1 and 2 refer to raft and background phases, respectively. Ref. 40 of the main text arrives at a similar free energy, but the differences in parameter values between raft and background phases in their work arise from a two-species Landau theory in terms of the area fraction of one of the virus species.

Minimizing F_{gen} with respect to θ and then θ_0 proceeds analogously to the virus case. With the boundary conditions $\theta(0) = 0$, $\theta(\alpha R) = \theta_0$, and $\theta(R) = 0$,

$$\theta(r) = \begin{cases} \theta_0 \frac{I_\nu(s_1)}{I_\nu(\alpha S_1)} & 0 \leq r \leq \alpha R \\ \theta_0 \frac{K_1(s_2)/K_1(S_2) - I_1(s_2)/I_1(S_2)}{K_1(\alpha S_2)/K_1(S_2) - I_1(\alpha S_2)/I_1(S_2)} & \alpha R \leq r \leq R, \end{cases} \quad [\text{S42}]$$

where I_ν and K_ν are modified Bessel functions of the first and second kind, respectively, of order ν . To prevent confusion of the latter for Frank constants, we define $k_j \equiv K_j t_j$, for $j \in \{1, 2\}$, as an effective 2D Frank elastic constant, where K_j

refers to the 3D Frank constant. The twist penetration depths are $\lambda_j \equiv \sqrt{k_j/D_j}$, which rescale the distances as $s_j = r/\lambda_j$ and $S_j = R/\lambda_j$. The maximum twist angle is

$$\theta_0 = \frac{k_1 q_1 - k_2 q_2}{\sqrt{D_1 k_1} \frac{I_0(\alpha S_1)}{I_1(\alpha S_1)} + \sqrt{D_2 k_2} \frac{K_0(\alpha S_2)/K_1(S_2) + I_0(\alpha S_2)/I_1(S_2)}{K_1(\alpha S_2)/K_1(S_2) - I_1(\alpha S_2)/I_1(S_2)}}. \quad [\text{S43}]$$

After integrating out θ , F_{gen} becomes

$$\frac{F_{\text{struct}}}{2\pi R_t^2} = \frac{\alpha}{R} \left\{ \gamma - \frac{1}{2} \frac{(k_1 q_1 - k_2 q_2)^2}{\sqrt{D_1 k_1} \frac{I_0(\alpha S_1)}{I_1(\alpha S_1)} + \sqrt{D_2 k_2} \frac{K_0(\alpha S_2)/K_1(S_2) + I_0(\alpha S_2)/I_1(S_2)}{K_1(\alpha S_2)/K_1(S_2) - I_1(\alpha S_2)/I_1(S_2)}} \right\}, \quad [\text{S44}]$$

a major result of the main text, but here for generalized membranes.

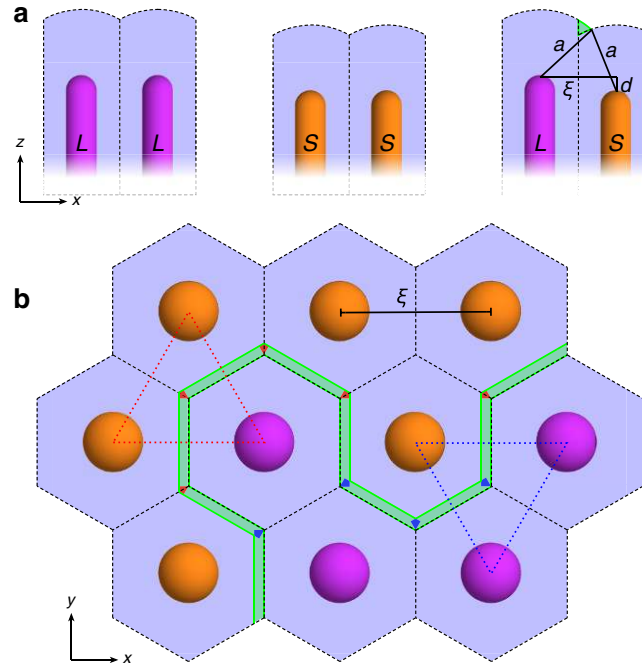


Fig. S1. An Ising-like model for depletion-induced phase separation in the limit of small virus half-length difference d . (A) A membrane composed of longer L viruses (Left) contains more excluded volume per particle (blue) than a membrane composed of shorter S viruses (Center), which leads to a linear term in the Ising-like Hamiltonian Eq. S21. A virus pair consisting of one L and one S particle (Right) occupies more excluded volume than the average of a pair of two L particles and a pair of two S particles. This extra excluded volume (green) has approximate cross-sectional area $ad^2/2\xi$ and leads to quadratic terms in Eq. S21. (B) Assuming a hexagonal lattice of viruses, a nearest-neighbor triplet consisting of one L virus and two S viruses (red dotted triangle, for example) produces slightly more excluded volume than a triplet consisting of two L viruses and one S virus (blue dotted triangle, for example). These small additions (dark red regions) and reductions (dark blue regions) in excluded volume contribute cubic terms in Eq. S21. Schematics are not drawn to scale.

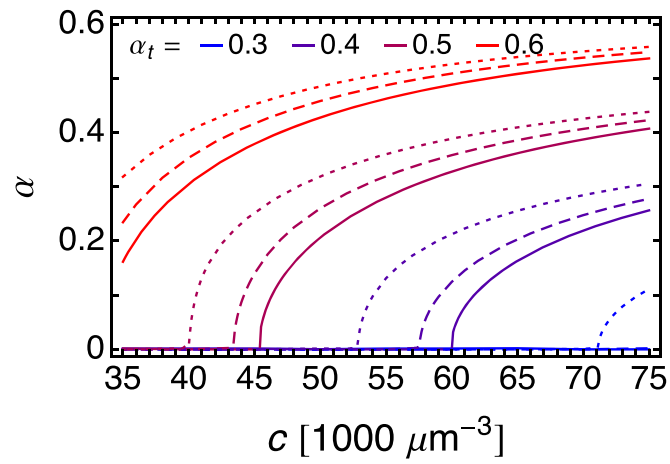


Fig. S2. Phase separation using a total free energy incorporating raft structure and organization. α^2 is the area fraction of the raft phase, and it is obtained by numerically minimizing the sum of Eqs. 4 and 13 of the main text over a range of depletant concentrations c . We use the same parameter values given in Table 1 of the main text, except that the chiral wavenumbers q_{fd} and q_{M13} are multiplied by a factor of 1 (solid lines), 2 (dashed lines), or 2.5 (dotted lines). The solid lines are indistinguishable from Fig. 2D of the main text, which plots Eq. 5. As the chiral wavenumber difference increases in magnitude past a critical value, α increases beyond its value in Eq. 5 and phase separation begins at lower values of c .

Correction

PHYSICS, BIOPHYSICS AND COMPUTATIONAL BIOLOGY

Correction for “Chiral twist drives raft formation and organization in membranes composed of rod-like particles,” by Louis Kang and Tom C. Lubensky, which was first published December 20, 2016; 10.1073/pnas.1613732114 (*Proc Natl Acad Sci USA* 114:E19–E27).

The authors note that a sign error for the $\frac{1}{2}\lambda_2^2\theta_0^2$ term in Eq. 9 caused the equation to appear incorrectly. The correct Eq. 9 is as follows:

$$\frac{F_{struct}}{4\pi caT} = \frac{R_t^2}{R^2} \left\{ d\alpha R - [\lambda_1^2 q_1 - \lambda_2^2 q_2] \alpha R \theta_0 + \frac{1}{2} [\lambda_1^2 - \lambda_2^2] \theta_0^2 \right. \\ \left. + \int_0^{aR} dr \left[\frac{1}{2} r \theta^2 + \frac{\lambda_1^2}{2} \left(r (\partial_r \theta)^2 + \frac{\theta^2}{r} \right) \right] \right. \\ \left. + \int_{aR}^R dr \left[\frac{1}{2} r \theta^2 + \frac{\lambda_2^2}{2} \left(r (\partial_r \theta)^2 + \frac{\theta^2}{r} \right) \right] \right\}$$

Additionally, in the Supporting Information, the same sign error caused Eqs. S4 and S5 to appear incorrectly. The correct Eq. S4 is as follows:

$$\frac{F_{domain}}{4\pi caT} = \frac{1}{2} R^2 + d\alpha' R' - [\lambda_1^2 q_1 - \lambda_2^2 q_2] \alpha' R' \theta_0 \\ + \frac{1}{2} [\lambda_1^2 - \lambda_2^2] \theta_0^2 \\ + \int_0^{aR'} dr \left[\frac{1}{2} r \theta^2 + \frac{\lambda_1^2}{2} \left(r (\partial_r \theta)^2 + \frac{\theta^2}{r} \right) \right] \\ + \int_{aR'}^{R'} dr \left[\frac{1}{2} r \theta^2 + \frac{\lambda_2^2}{2} \left(r (\partial_r \theta)^2 + \frac{\theta^2}{r} \right) \right]$$

The correct Eq. S5 is as follows:

$$\frac{F_{domain}}{4\pi caT} = \frac{1}{2} R^2 + d\alpha R - [\lambda_1^2 q_1 - \lambda_2^2 q_2] \alpha R \theta_0 \\ + \frac{1}{2} [\lambda_1^2 - \lambda_2^2] \theta_0^2 \\ + \int_0^{aR} dr \left[\frac{1}{2} r \theta^2 + \frac{\lambda_1^2}{2} \left(r (\partial_r \theta)^2 + \frac{\theta^2}{r} \right) \right] \\ + \int_{aR}^R dr \left[\frac{1}{2} r \theta^2 + \frac{\lambda_2^2}{2} \left(r (\partial_r \theta)^2 + \frac{\theta^2}{r} \right) \right]$$

Also in the Supporting Information, a sign error for the $\frac{1}{2}K_2t_2\theta_0^2$ term in Eq. S41 caused the equation to appear incorrectly. The correct Eq. S41 is as follows:

$$\frac{F_{gen}}{2\pi} = \frac{R_t^2}{R^2} \left\{ \gamma \alpha R - [K_1 t_1 q_1 - K_2 t_2 q_2] \alpha R \theta_0 \right. \\ \left. + \frac{1}{2} [K_1 t_1 - K_2 t_2] \theta_0^2 \right. \\ \left. + \int_0^{aR} dr \left[\frac{D_1}{2} r \theta^2 + \frac{K_1 t_1}{2} \left(r (\partial_r \theta)^2 + \frac{\theta^2}{r} \right) \right] \right. \\ \left. + \int_{aR}^R dr \left[\frac{D_2}{2} r \theta^2 + \frac{K_2 t_2}{2} \left(r (\partial_r \theta)^2 + \frac{\theta^2}{r} \right) \right] \right\}$$

The SI has been corrected online.

Published under the [PNAS license](#).

Published online August 6, 2018.

www.pnas.org/cgi/doi/10.1073/pnas.1812385115